iScience

CellPress
OPEN ACCESS

Article

Prolactin blood concentration relies on the scalability of the TIDA neurons' network efficiency *in vivo*

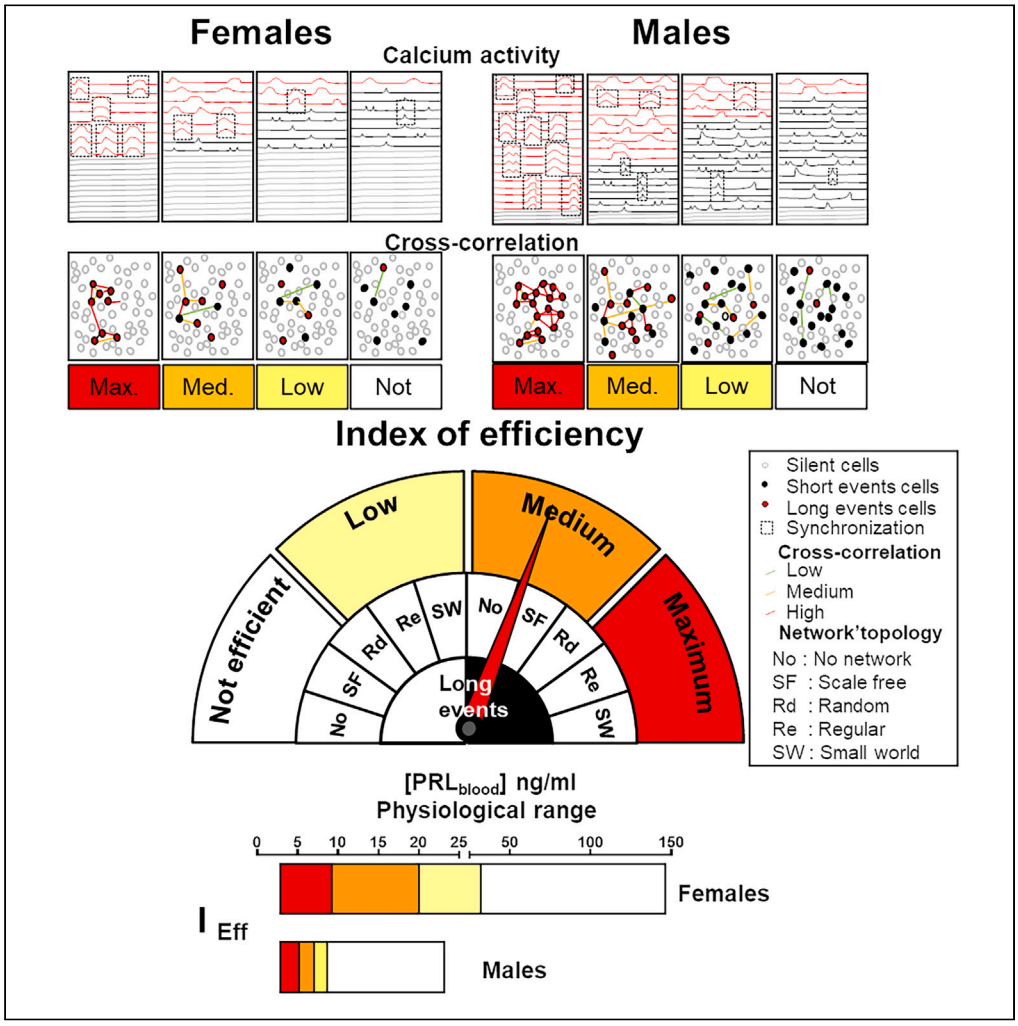

Stanislav Cherepanov, Louise Heitzmann, Pierre Fontanaud, ..., Pauline Campos, Patrice Mollard, Agnès O. Martin

agnes.martin@igf.cnrs.fr

Highlights

TIDA neurons, organize as dynamic functional networks both in and *ex vivo*

The plasticity of networking efficiency allows modulation of [PRL$_{blood}$]

The sex-specific number of active TIDA contributes to the [PRL$_{blood}$] sexual dimorphism

Cherepanov et al., iScience *27*, 109876
June 21, 2024
https://doi.org/10.1016/j.isci.2024.109876

iScience

CellPress
OPEN ACCESS

Article

Prolactin blood concentration relies on the scalability of the TIDA neurons' network efficiency *in vivo*

Stanislav Cherepanov,[1] Louise Heitzmann,[2] Pierre Fontanaud,[1] Anne Guillou,[1] Evelyne Galibert,[1] Pauline Campos,[3] Patrice Mollard,[1] and Agnès O. Martin[1,4,*]

SUMMARY

Our understanding and management of reproductive health and related disorders such as infertility, menstrual irregularities, and pituitary disorders depend on understanding the intricate sex-specific mechanisms governing prolactin secretion. Using *ex vivo* experiments in acute slices, in parallel with *in vivo* calcium imaging (GRIN lens technology), we found that dopamine neurons inhibiting PRL secretion (TIDA), organize as functional networks both in and *ex vivo*. We defined an index of efficiency of networking (I_{eff}) using the duration of calcium events and the ability to form plastic economic networks. It determined TIDA neurons' ability to inhibit PRL secretion *in vivo*. I_{eff} variations in both sexes demonstrated TIDA neurons' adaptability to physiological changes. A variation in the number of active neurons contributing to the network explains the sexual dimorphism in basal [PRL]blood secretion patterns. These sex-specific differences in neuronal activity and network organization contribute to the understanding of hormone regulation.

INTRODUCTION

Prolactin (PRL) secretion is highly sexually dimorphic in basal conditions[1] and displays sex-specific physiological modification of its secretory pattern (estrous cycle, gestation, lactation). Hypo- and hyperprolactinemia are common types of PRL secretion dysregulations, inducing sexual and reproductive life debilitating symptoms for both sexes (impotence, hypo-spermatogenesis, loss of libido in males, amenorrhea, and cessation of normal cyclic ovarian function in females).[2,3] Understanding the underlying logic of PRL regulatory systems and their sexual dimorphism is critical to treat these disorders.

To maintain homeostasis, hormonal secretion requires robust and plastic processing in the face of highly dynamic environments and inputs. The temporal pattern of PRL release relies almost uniquely on the timing of the inhibitory tone exerted by dopamine (DA) that is secreted by tuberoinfundibular dopamine (TIDA) neurons in the arcuate nucleus. TIDA neurons project to the median eminence (ME), where they secrete DA onto the fenestrated blood vessels of the pituitary portal system.[4,5] PRL regulates its secretion through direct activation of PRL receptors (PRL-R) on TIDA neurons[6,7] by classical short-loop negative feedback.[8,9] All TIDA neurons show transcriptional responses to PRL,[10,11] leading to enhanced activity of the tyrosine-hydroxylase (TH) and increased synthesis of DA. In addition, we and others showed that PRL exerts a direct modulation of the TIDA neurons' functionality. The PRL-induced increased electrical activity participates directly in the modulation of the TIDA neurons' physiological output and results in increased DA release.[12] We previously described the *in vivo* temporal organization of DA release at the ME in freely moving mice.[13] We showed that DA release events are repeated over weeks as network-driven rhythms that cover more than four orders of magnitude of frequency, from infraslow (<0.001 Hz) to fast rhythms (1–10 Hz). This organization of the TIDA neurons output suggested the presence of harmonization of the functional properties of the TIDA neurons to generate the rhythm of DA secretion.[13] *Ex vivo* studies revealed some levels of harmonization in calcium and electrophysiological properties of the TIDA neurons and modifications of these characteristics during lactation but failed to identify any difference between sexes or modulation explaining the plasticity of the PRL secretion in basal physiological conditions.[12,14,15]

What is the *in vivo* organization of TIDA neurons remains unresolved. Here, we provided the first *in vivo* study of the TIDA neurons' calcium activity and defined a scalable index of TIDA neuron network functioning that tightly reflects [PRL_{blood}] variations.

RESULTS

The pattern of PRL secretion varies as a function of the physiological state and is highly sexually dimorphic, with females presenting mean levels 10 times higher than males (32.26 ng/mL ± 3.17 ng/mL (n = 50) and 4.9 ± 0.67 ng/mL (n = 18); (Student's t test, $p < 0.0001$). (Figure 1A

[1]Team for networks and rhythms in endocrine glands. Institute of Functional Genomics, CNRS, INSERM. Montpellier, 34094 Occitanie, France
[2]Sex and speciation team, department of genome, phenome and environment. Montpellier Institute of Evolution Science, CNRS. Montpellier, 34090 Occitanie, France
[3]Department of Mathematics and Statistics, Faculty of Environment, Science and Economy, University of Exeter, Exeter, UK
[4]Lead contact
*Correspondence: agnes.martin@igf.cnrs.fr
https://doi.org/10.1016/j.isci.2024.109876

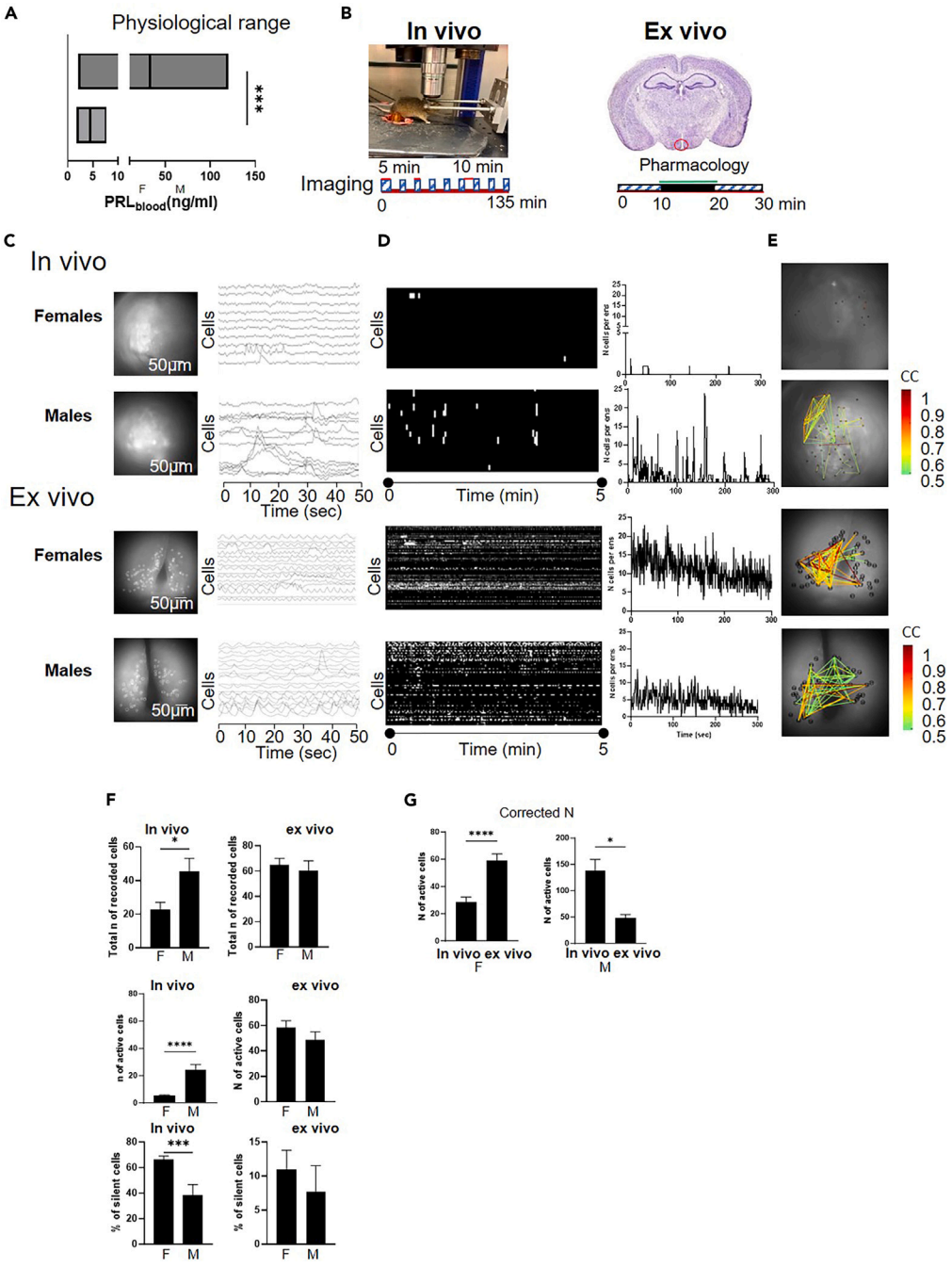

Figure 1. *In vivo* calcium imaging demonstrates difference between sexes of TIDA activity, which disappear *ex vivo*

(A) [PRL]$_{blood}$ DAT-iCRE- GCAMP6f virgin females (n = 50) and males (n = 18) mice.

(B) Left panel: representative image of *In vivo* head-fixed experiment condition and protocol of recording. DAT-iCRE- GCAMP6f mice were recorded during 135 min, first control recording of 10 min, following recording lasting 5 min, with 10 min pause. Blue-hatched rectangles: episodes of imaging. Right part—representative image of brain slice for *ex vivo* experiments. Red circle indicated area of recording—Nucleus Arcuate and Medium Eminence. Continuous imaging for 30 min, 5 min of control recording was analyzed.

(C) Representative images of recordings (left). Tracks of calcium waves (Right). Tracks represent normalized F/F0 Calcium Waves.

(D) Representative images of on/off raster-plots (left) and coactivity plots (right) (E) Representative images of cross-correlation functional networks.

(F) From top to bottom: total number of recorded cells; number of active cells in control recordings; % of silent cells in control recordings; left panel for *in vivo* experiments females (n = 50) and males (n = 22), right panel for *ex vivo* (n = 22) for females and (n = 7) for males, respectively.

(G) Predicted active cell number in control recording for females in left and males in right panel. Student unpaired two-tailed t test used for comparison of 2 groups. For correlation analysis Pearson coefficient. *p < 0.05, ***p < 0.001, ****p < 0.00001.

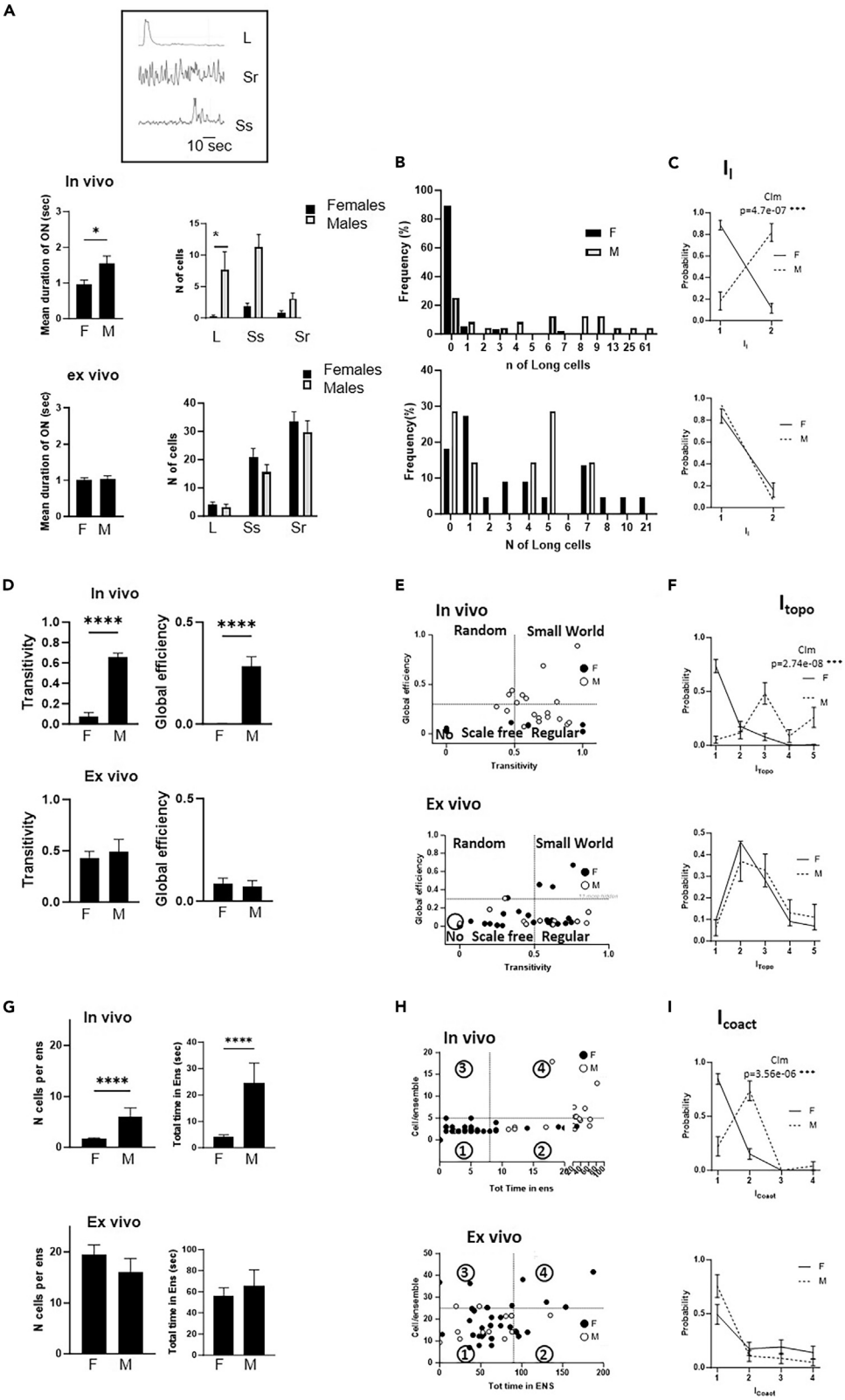
A
L
Sr
Ss
10 sec
In vivo
Mean duration of ON (sec)
F M
N of cells
L Ss Sr
Females
Males
ex vivo
B
Frequency (%)
F
M
n of Long cells
Frequency(%)
N of Long cells
C
I_l
Clm
p=4.7e-07 ***
Probability
I_l
D
In vivo
Transitivity
Global efficiency
****
Ex vivo
E
In vivo
Random
Small World
No Scale free Regular
Global efficiency
Transitivity
Ex vivo
F
I_{topo}
Clm
p=2.74e-08 ***
I_{topo}
G
In vivo
N cells per ens
Total time in Ens (sec)
Ex vivo
H
In vivo
Cell/ensemble
Tot Time in ens
Ex vivo
Tot time in ENS
I
I_{coact}
Clm
p=3.56e-06 ***
I_{coact}

Figure 2. Presence of long calcium waves, regular or small-world topology of functional networks and high coactivity of cells are different between sexes *in vivo*

(A Left) Mean duration of ON for control experiments on males and females *in vivo* (top) and *ex vivo* (bottom). For *in vivo* experiments females ($n = 52$) and males ($n = 22$), for *ex vivo* (females $n = 22$) and (males $n = 7$). (A Insert) Representative image of three types of calcium activity. Long (L) duration >1.75 s; short rapid (Sr) duration <1.75 s, frequency >75mHz; short slow (Ss) duration <1.75 s, frequency <75 mHz. (A right) Number of cells producing each type of waves *in vivo* (Top) and *ex vivo* (Bottom) *In vivo* experiments females ($n = 52$) and males ($n = 22$), for *ex vivo* ($n = 22$) for females and ($n = 7$) for males. Data pooled from all control recordings.

(B) Frequency distribution (%) of the number of recordings presenting Long cells, *in vivo* (Top) and *ex vivo* (Bottom).

(C) Probability for recordings to belong to different Index Long (I_L). IL = 1 represent recordings with no recorded cells exhibiting L calcium activity. $I_L = 2$ recordings with number of L ≥ 1. CLM model demonstrate high probability to belong to $I_L = 2$ in males compared to females *In vivo* (Top) but not *Ex vivo* (Bottom).

(D) Mean transitivity and global efficiency for *in vivo* (top) and *ex vivo* (bottom) in male and female groups. *in vivo* experiments females ($n = 41$) and males ($n = 20$), for *ex vivo* ($n = 22$) for females and ($n = 7$) for males.

(E) Types of functional network *in vivo* (top) end *ex vivo* (bottom). Each dot represents control recording for individual animal for *in vivo* experiment and control recording for each brain slice for *ex vivo* experiments.

(F) Probability for recordings to belong to different "Index topology » (I_{topo}). $I_{topo} = 1$ absence of functional network, 2—scale free network, 3—Regular network, 4—Random network, 5—Small world network. CLM model demonstrate significant difference between males and females *in vivo* (Top) but not *Ex vivo* (Bottom).

(G) Number of cells per coactive ensemble and total time in ensemble of coactive cells for *in vivo* (top panel) and *ex vivo* experiments (bottom panel).

(H) Pooled data of types of functioning of coactive networks for *in vivo* (top panel) and *ex vivo* experiments (bottom panel).

(I) Probability of recordings to belong to different Index of coactivity (I_{coact}). CLM model demonstrate difference between females and males *In vivo* (Top panel) but not *Ex vivo* (Bottom panel). Student unpaired two-tailed t test used for comparison of 2 groups. For correlation analysis Pearson coefficient. CLM model used for indexes as categorical data. $^*p < 0.05$, $^{**}p < 0.01$, $^{***}p < 0.001$.

and Table S2).[1] The total number of used animals and recordings of each animal are provided in Table S1. Examples of GRIN-lens anatomical positions are presented in Figure S1. The physiological range of $[PRL]_{blood}$ was wider in females (with a range of 117.6 ng/mL (from 2.15 ng/mL to 120 ng/mL) than in males (range 6 ng/mL [from 1.8 ng/mL to 8 ng/mL]). The acquisition protocol for calcium imaging was designed to limit phototoxic damage (Figure 1B). Single-cell gCAMP6f fluorescence was identified in the recording field, defined as a single region of interest (ROI) (FiJI ROI manager) (Figure 1C left). *In vivo*, the number of observable cells in the gradient index (GRIN) lens field (i.e., cells presenting detectable basal fluorescence for gCamp6f) presented a difference between sexes, with on average 22.8 $\pm$ 4.2 cells ($n = 11$) and 45.3 $\pm$ 7.8 cells ($n = 10$) (Student's t test, $p < 0.05$) identifiable neurons in females and males, respectively (Figure 1F, top left). *Ex vivo*, the number of recordable cells was not significantly different between females and males. (65 $\pm$ 5.2 cells [$n = 31$] and 60.1 $\pm$ 7.5 cells [$n = 18$] in females and males, respectively) (Student's t test) (Figure 1F, top right).

The number of spontaneously active cells is a hallmark of TIDA neurons' sex-difference *in vivo*

In vivo, the number of spontaneously active cells (N) was drastically lower in females compared to males (5.3 $\pm$ 0.53 cells ($n = 60$) and 24.3 $\pm$ 3.78 cells ($n = 22$) (Student's t test $p < 0.0001$)) (Figure 1F, middle left, and Table S2). A large proportion of neurons remained silent, with a significantly higher percentage in females (67.6% $\pm$ 2.6 [$n = 60$] and 38% $\pm$ 8.6 [$n = 10$] in females and males, respectively, Student's t test $p = 0.0004$) (Figure 1F, bottom left). Examples of recordings for females (diestrus phase) and males are presented in the supplement (see Videos S1 and S2). The number of spontaneously active cells *ex vivo* lacked sexual difference (58.73 $\pm$ 5.07 cells [$n = 22$] in females vs. 48.43 $\pm$ 6.86 cells [$n = 7$] in males) (Figure 1F, middle right, and Table S1), and the percentage of silent cells was low (11.53 and 7.71% for females and males, respectively). (Figure 1F bottom right). Examples of *ex vivo* recordings of female mice (diestrus phase) are presented in supplementary data (see Video S3). We corrected the number of active cells *in vivo* (to match field recording size, in and *ex vivo*) to directly compare the level of active cells in both conditions for each sex. In females, the number of active cells *ex vivo* was significantly higher than the corrected number *in vivo* (58.7 $\pm$ 5.07 cells [$n = 22$] vs. 28.8 $\pm$ 3.3 cells [$n = 54$), Student's t test, $p < 0.0001$) (Figure 1G, left). Conversely, in males, the number of active cells *ex vivo* was significantly lowered (48.4 $\pm$ 6.7 cells, [$n = 7$] vs. 138 $\pm$ 48.4 cells, [$n = 22$], unpaired t-test, $p = 0.013$) (Figure 1G, right). The recorded waves (Figure 1C right) were binarized (see STAR Methods) to generate a raster of single-cell periods of spontaneous activity (ON) and silence (OFF) (Figure 1D).

Single TIDA neurons can be classified into categories based on the duration and frequency of calcium events

Total time on ON (TOTAL ON [sec]), frequency of ON, and average duration of single ON (Mean duration ON) were extracted from ON/OFF rasters. Male TIDA neurons displayed an increased duration of single events (1.55 $\pm$ 0.21 s) ($n = 22$) compared to females (0.95 $\pm$ 0.13 s) ($n = 52$), Student's t test $p = 0.0005$) (Figure 2A top, Table S2). This female/male difference was lost *ex vivo* (Figure 2A, bottom, Table S2). No sexual difference was found for the total time in ON and frequency of ON in both conditions (Table S2).

We classified spontaneous calcium activity according to the mean duration of ON and frequency: long (L), short/slow frequency (Ss), and short/rapid frequency (Sr) (Figure 2A, insert, and Table S3).

In vivo, the number of neurons in each cluster was different between sexes, with males' recordings showing significantly longer events than females (0.3077 $\pm$ 0.15 cells [$n = 52$] recordings for females, 7.68 $\pm$ 2.83 cells ($n = 22$) recordings for males, $p = 0.0001$, Student's t test). (Figure 2A, top right, and Table S2). No sex difference was detected in acute slices (Figure 2A, bottom right, and Table S2).

Recordings were classified into two groups according to the presence or absence of cells presenting long events: $N_{Long\ events\ cells} = 0$ (1) or $N_{Long\ events\ cells} > 0$ (2) (Index Long: I_l). *In vivo*, the probability of belonging to $N_{Long\ events\ cells} > 0$ was significantly higher in males compared to females ($z = 5.04$, $p = 4.7e\text{-}07$) (Figure 2C Top), while no difference was observed *ex vivo* (Figure 2C Bottom). *Ex vivo*, in both sexes, the probability of belonging to I_l $N_{Long\ events\ cells} > 0$ was comparable to male TIDA neurons *in vivo*.

Functional activity of TIDA neurons organized as sex-different topological network *in vivo*

We then explored whether TIDA neurons were functionally connected using cross-correlation between the total calcium activity of individual cells.[16–19] Transitivity (T) and global efficiency (E_{glob}) were used to define network topology. Examples of maps of functional networks based on cross-correlation between cells are shown in Figures 1E and S2.

In vivo, both T and E_{glob} were higher in males versus females (with $T = 0.66 \pm 0.037$ [$n = 20$] vs. $T = 0.07 \pm 0.04$ [$n = 41$], Student's t test, $p < 0.0001$; and $E_{glob} = 0.28 \pm 0.04$ [$n = 20$] vs. Eglob $\pm$0.001 [$n = 41$], Student's t test, $p < 0.0001$) (Figure 2D Top left and right and Table S2).*Ex vivo*, both parameters were not significantly different (Table S1; Figure 2D Right). We defined 5 types of network topology in the recordings, which were based on both T and E_{glob} values (with if T and $E_{glob} = 0$, no network if $0 < T < 0.5$ and $0<Eglob<0.3$: scale-free network, if $T > 0.5$ and $0<Eglob<0.3$, regular network, if $0 < T < 0.5$ and $Eglob>0.3$, random network, if $T > 0.5$ and $Eglob>0.3$, small word network) (index of topology (I_{topo}) (Figure 2E and Table S3).

In vivo, males differed from females ($z = 5.56$, $p = 2.74e\text{-}08$) (Figure 2F top), with males presenting all 5 categories of networks, while in females, a lack of network organization (no network category) represented the majority of recordings. Scale-free and random networks were present in limited proportions. *Ex vivo* probability for a recording to belong to different categories was not different between sexes, with a majority of recordings under scale-free and regular configurations, with very little proportion of no network (Figure 2F bottom).

The size and temporal weight of the coactive network are different between males and females *in vivo*. The number of TIDA neurons presenting long-lasting calcium events, network topology, and level of coactivity correlated with basal $[PRL]_{blood}$

In vivo, N, I_l, I_{topo}, and I_{coact} presented differences between the sexes. We tested whether these parameters were correlated with the $[PRL]_{blood}$ of samples collected while TIDA neurons were recorded. When females were pooled together, N, I_l, I_{topo}, and I_{coact} displayed a negative correlation of increased strength and significance with $[PRL]_{blood}$ (Pearson's $r = -0.36$, $p = 0.0026$, $r = -0.51$, $p = 0.000009$, $r = -0.49$, $p = 0.0001$, and $p = -0.39$, $p = 0.001$, respectively) (Figures 3A–3D). When both sexes were considered separately, the correlation was lost for N (Figure 3A, middle and right) and I_{coact} (Figure 3D, middle and right). Meanwhile, I_l and I_{topo} showed a significant correlation with $[PRL]_{blood}$ for both sexes, with the negative correlation being stronger and more significant in males (Figures 3B and 3C, middle and right).

The three indexes, I_l. I_{topo} and I_{coact} were combined to provide a single number. For example, cluster 234 presented $N_{Long\ events\ cells} > 0$ ($I_l = 2$), regular network ($I_{topo} = 3$), and $I_{coact} = 4$. *In vivo*, the frequency distribution of recordings in the different clusters was highly different between the sexes (Figure 4A). *Ex vivo*, the sex difference in frequency distribution was lost (data not shown).

We classified the clusters into 4 groups of theoretically increasing efficiency (index of efficiency, I_{eff}). Clusters 111 to 114 were identified as not efficient, clusters 121 to 124, as low efficiency, clusters 131 to 224, as medium efficiency, and 231 to 254 as maximum efficiency (Figures 4A and S2; Table S3 for examples). Under this classification, a significant difference between sexes was observed *in vivo* ($z = 5.7$, $p = 1.29e\text{-}08$) (Figure 4B Left). TIDA neurons in females mostly displayed not efficient I_{eff} (probability $= 0.7 \pm 0.06$) with a small proportion of medium and maximum efficiency networks (probability $= 0.12 \pm 0.04$ and 0.04 ± 0.02), while in males, TIDA neurons presented mainly medium and maximum efficiency (0.23 ± 0.07 and 0.7 ± 0.1) (Figure 4B Left). No difference between sexes was observed *ex vivo* (Figure 4B, right), with a very low amount of not efficient network, a large majority of recordings being of low and medium efficiency, and a notable part being of maximum efficiency.

In vivo, I_{eff} displayed a strong negative correlation with $[PRL]_{blood}$ in both sexes (Pearson's $r = -0.40$, $p = 0.004$, and -0.75, $p = 0.0004$ for females and males) (Figure 4C).

Modification of index of efficiency (I_{eff}) reflects $[PRL]_{blood}$ temporal plasticity *in vivo*

We analyzed separately male recordings displaying low (<5 ng/ml) or high (≥5 ng/ml) $[PRL]_{blood}$ (*in vivo* male's mean $[PRL]_{blood}$ levels being 4.9 ng/m $\pm$0.68) (Table S4) (Figure 5A). We show examples of raster ON/OFF, coactivity, and functional networks (Figures 5B and 5C). The general level of population activity was not modified (Figure 5D and Table S4). In low-level PRL recordings, the duration of the ensemble was significantly increased (4.18 ± 0.98 s [$n = 8$] and 1.69 ± 0.23 s [$n = 8$], $p = 0.026$ unpaired t-test), the number of cells presenting long events tended to increase (11.7 ± 5.9 cells [$n = 8$] and 4.62 ± 1.4 cells [$n = 8$], $p = 0.31$ unpaired t-test). These subtle modifications were sufficient to induce a shift toward maximum efficiency in low PRL males (frequency = 1 versus 0.57 for high PRL males (Fisher's Exact Test, $p = 0.06$) (Figure 5E).

To study the possible role of I_{eff} modifications on $[PRL]_{blood}$ variations over time, a male was recorded for 5 min daily for 9 consecutive days with coupled blood sampling. Daily fluctuation of $[PRL]_{blood}$ was strongly correlated with modification of I_{Eff}. (Pearson's $r = -0.74$, $p = 0.02$) (Figure 5F), suggesting that I_{Eff} reflects $[PRL]_{blood}$.

I_{eff} changes reflected $[PRL]_{blood}$ modulation during the estrous cycle

$[PRL]_{blood}$ was modulated with a marked decrease during estrus compared to other stages.[16] In our conditions, the mean $[PRL]_{blood}$ was 41.05 ± 5.9 ng/mL ($n = 25$) for diestrus and 12.08 ± 2.7 ng/mL ($n = 13$) ($p = 0.0017$, Student's unpaired t-test) during estrus (Figure 5G).

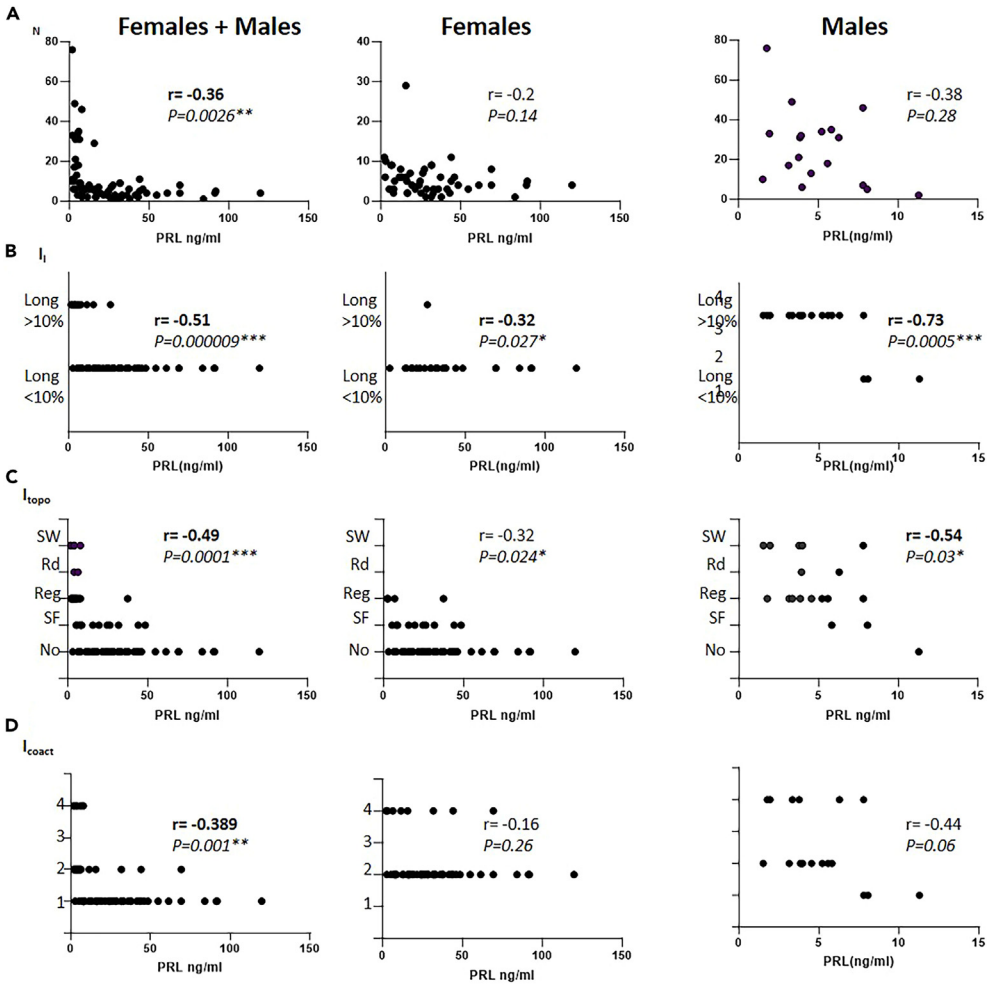

Figure 3. Number of active cells, I_I, I_{topo} and I_{coact} clusters displayed a strong negative correlation with prolactin levels in blood

(A) Number of active cells in control recordings correlated with [Ca^{2+}] for combined males and females' groups (left) but not for females (Center) and males (Right) separately.

(B) IL was correlated with prolactin levels in blood both in combined (left) and separated females (center) and males (right) groups.

(C) I_{topo} was correlated with prolactin levels in blood both in combined (left) and separated females (center) and males (right) groups.

(D) I_{coact} was correlated with prolactin levels in blood for combined males and females' groups (left) but not for females (Center) and males (Right) separately. Each dot represents control recording for individual animal. For correlation analysis Pearson coefficient was used. $^{**}p < 0.01$, $^{***}p < 0.001$.

The basic level of activity (n of active cells and % of silent cells) was not different between estrus and diestrus either *in vivo* or *ex vivo* (Figure 5J, Table S4) (see Videos S1 and S3). Examples of raster ON/OFF, coactivity, and functional networks are shown in Figures 5H and 5I.

The coactivity network of TIDA neurons *in vivo* was modified during the estrous cycle, with an increased number of Ens (4.26 $\pm$ 1 [n = 13] and 1.76 $\pm$ 0.5 [n = 25], p = 0.0074, Student's t test), n cells per Ens (2.7 $\pm$ 0.25 [n = 13] and 1.27 $\pm$ 0.3 [n = 25], p = 0.0017, Student's t test), and Total time in Ens (9.92 $\pm$ 2.12 [n = 13] and 2.27 $\pm$ 0.63 [n = 25], p = 0.0001, Student's t test) during estrus (Table S4). Despite these differences, the probabilities of belonging to the different (I_{coact}) were not modified during the estrous cycle (data not shown). No modifications of the coactivity parameters were observed *ex vivo*.

E_{glob} and T were unchanged between both estrous cycle stages, both in and *ex vivo* (Table S4) and (I_{topo}), therefore, did not show a significant difference between estrous cycle stages (data not shown).

Average duration of ON was significantly increased during estrus *in vivo* 1.5 $\pm$ 0.45 s [13] vs. 0.76$\pm$-0.08 [25] Student's t test (p = 0.0337) (Table S4). This translated into a significant increase in the number of long events cells during estrus (1.07 $\pm$ 0.54 cells) (n = 13) compared with diestrus (0.04 $\pm$ 0.04 cells, [n = 25] unpaired t-test p = 0.02) (Figure 5K right and Table S4). Categorization into (I_L) illustrated the decrease of n of long events cells during diestrus, with a significant difference in the probability of belonging to each cluster between sexes *in vivo* (z = 2.37, p = 0.02) (Figure 5K Left).

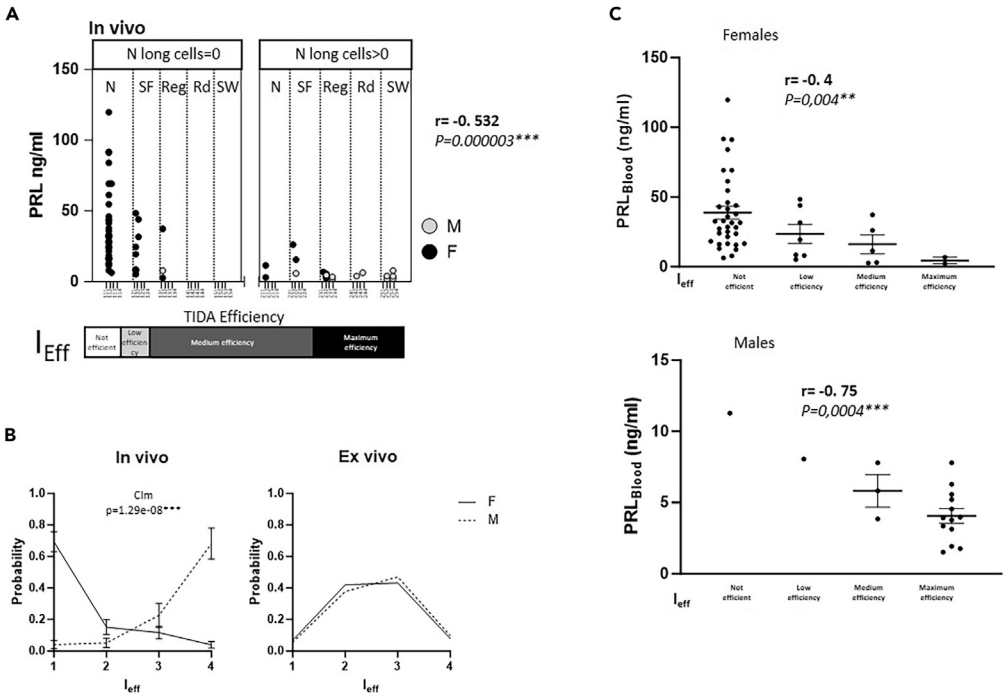

Figure 4. Combination of I_l, I_{topo} and I_{coact}, predicts high efficiency of TIDA to suppress prolactin release

introduction of I_{eff} model.

(A Top) Distribution of combinations of I_L, I_{topo} and I_{coact} for *in vivo* experiments and correlation with $[PRL]_{blood}$. Data pooled from control recordings of mice of both sexes. (gray dots for males and white for females) (A insert) Corresponding classification in I_{eff}.

(B) Probability of recordings to belong to different I_{eff} value. CLM model demonstrate significant difference of I_{eff} *in vivo* (Left) but not *ex vivo* (Right).

(C) I_{eff} was correlated with prolactin levels in blood, both in females (top) and males (bottom) groups. For correlation analysis Pearson coefficient was used. CLM model used for indexes as categorical data. $^{**}p < 0.01$, $^{***}p < 0.001$.

Classification with I_{eff} was significantly different between estrus and diestrus ($z = 2.15$, $p = 0.032$), with a shift toward the inefficient group during diestrus, and toward the maximum efficiency cluster in estrus (Figure 5L). I_{Eff} was negatively and significantly correlated with $[PRL]_{blood}$ (Pearson's $r = -0.39$, $p = 0.01$) (Figure 5M).

Blood was sampled at the end of each calcium imaging recording, over two consecutive estrous cycles on a single animal. $[PRL]_{blood}$ varied over time, with characteristically lower levels during estrus (Figure 5N). Longitudinal changes in $[PRL]_{blood}$ were paralleled with modifications of I_{Eff} with a strong and significant negative correlation between I_{Eff} and $[PRL]_{blood}$ (Pearson's $r = -0.63$, $p = 0.02$).

Experimentally induced low circulating PRL blood levels silenced TIDA neurons *in vivo*

To test the effect of low levels of $[PRL]_{blood}$, the same animals were recorded before and after treatment with bromocriptine (i.p single injections daily for 2 days). It induced a drastic reduction in $[PRL]_{blood}$ both in females (from 24.36 ± 3.2 ng/mL to 3.54 ± 1.1 ng/mL, $p = 0.015$ ($n = 3$) (Figure 6A Top Left) and males (from 3.54 ± 1.1 ng/mL to 1.2 ± 0.2 ng/mL ($n = 3$; Student's one-tailed t-test for paired data, $p = 0.027$) (Figure 6A Bottom Left). We show examples of raster ON/OFF, coactivity, and functional networks (Figure 6A, right). The number of active cells was reduced in both sexes, in females from 6.2 ± 1.7 cells to 2.8 ± 0.73 cells (Student's one-tailed t-test for paired data, $p = 0.03$, $n = 3$) (Figure 6B Top) and in males from 25.7 ± 4.2 cells to 7.25 ± 2.1 cells (Student's one-tailed t-test for paired data, $p = 0.02$, $n = 3$) (Figure 6B Bottom).

An acute increase in $[PRL]_{blood}$ induced transient and moderate reorganization of TIDA neurons network toward higher efficiency *in vivo*

In vivo, a transient surge of PRL was induced by an i.p. injection of either oPRL or the D2 DA receptor antagonist domperidone.[1] Both induced comparable modifications in TIDA neurons' calcium activity. Longitudinal recordings in control conditions (saline injection) did not induce modifications in calcium activity, results are presented in Table S5.

Domperidone induced a strong increase in $[PRL]_{blood}$ both in females (84.5 ± 9.36 ng/mL and 70.1 ± 10.27 ng/mL, 10 and 40 min after injection, compared to 31.09 ± 11.32 ng/mL, $n = 3$) and males (31.43 ± 7 ng/mL and 12.6 ± -5 ng/mL), 10 and 40 min after injection, compared to 5.9 ± 1.9 ng/mL, $n = 2$) (Figure 6D). Examples of cell activity before, 10 min, and 40 min after domperidone injection are presented in Figure 6C.

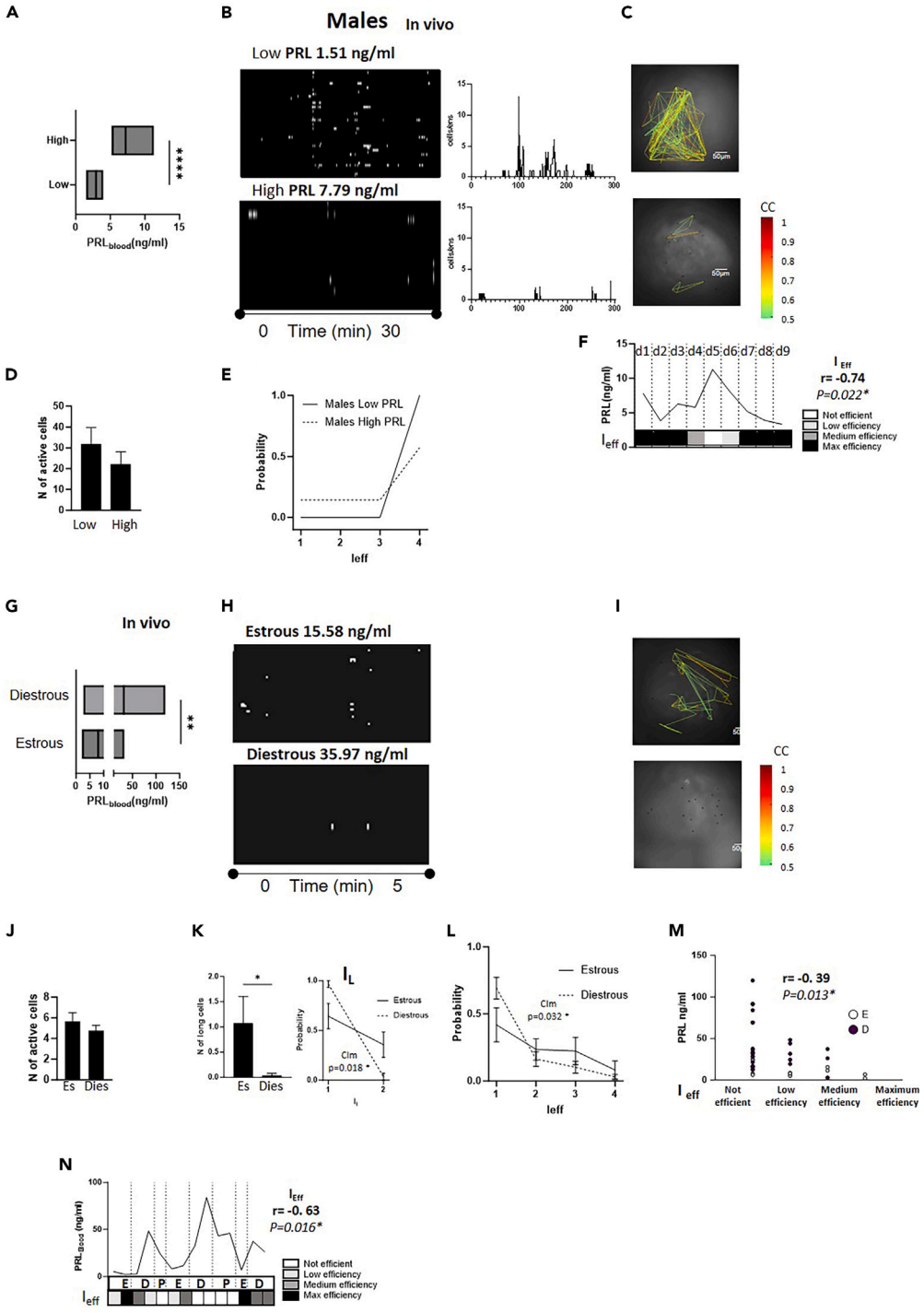

Figure 5. Presence of long type of calcium activity predicts efficiency of TIDA to decrease $[PRL]_{blood}$

(A) $[PRL]_{blood}$ in males classified in low ($[PRL]_{blood}$<4 ng/ml) and high ($[PRL]_{blood}$>4 ng/ml). Each dot represents individual recording followed blood sampling for males' group with low Prolactin level (n = 8), similar high Prolactin level (n = 8).

(B) Representative images of on/off raster-plots (Left), coactivity plots (Right) and (C) cross-correlation functional networks for males with low (top) and high levels (bottom) of prolactin.

(D) Number of active cells not different in "low" and "high" PRL males.

(E) Probability to belong to different I_{eff} class CLM model did not show the difference between two groups.

(F) Longitudinal study of a Male $[PRL]_{blood}$ sampled for 9 consecutive days, demonstrates significant correlation of I_{eff} and levels of prolactin.

Figure 5. *Continued*

(G) Levels of prolactin in blood in females (left) blood sampling for estrous phase $n = 13$, for Diestrous $n = 25$.

(H) Representative images of on/off raster-plots, (I) and cross-correlation functional networks for female mice in Estrous and Diestrous phase of estrous cycle.

(J) N of active cells *in vivo* experiments.

(K Left) Number of cells presenting Long events in estrus and diestrous phases of Estrous cycle. (K Right) Probability to belong to different I_L class *in vivo* (left), Estrous ($n = 13$) and Diestrous ($n = 25$). CLM demonstrates significant decrease of long events in Diestrous.

(L) Probability to belong to the different I_{eff} classes. CLM illustrated the significant shift to inefficient group during diestrous phase (M) Modifications of I_{eff} correlate with prolactin levels in blood. Each dot represents individual recording followed blood sampling.

(N) Longitudinal study of estrous cycle, I_{eff} and $[PRL]_{blood}$ demonstrated significant correlation of I_{eff} and levels of prolactin. In female mice observed during 14 consecutive days. Student unpaired two-tailed t test used for comparison of 2 groups. For correlation analysis Pearson coefficient. CLM model used for indexes as categorical data. *$p < 0.05$, **$p < 0.01$, ****$p < 0.00001$.

In females (Figure 6E top), 4 parameters displayed a significant increase between the control phase and 10 min after PRL elevation: duration of ON (2.03 ± 0.35 s ($n = 6$) vs. 0.95 ± 0.22 s ($n = 6$), $p = 0.01$, one way ANOVA Sidac test correction), total time ON (3.72 ± 0.4 s ($n = 6$) vs. 2 ± 0.48 s $p = 0.04$ ($n = 6$), post-hoc Sidak test, $p = 0.01$), n of long cells (5.8 ± 2.2 cells ($n = 6$) vs. 1.2 ± 1.2 cells ($n = 6$); post-hoc Sidak test, $p = 0.03$) and total time in Ens (24.5 ± 8.35 s ($n = 6$) vs. 7.67 ± 4.58 s ($n = 6$); Post-hoc Sidak test, $p = 0.02$). In males, no modifications of single cell, networking, or clustering properties were observed (Figure 6E bottom and Table S5). I_L, I_{coact}, I_{topo}, and I_{eff} were not significantly modified (Figure 6F) in both sexes.

Ex vivo, PRL synchronized TIDA neurons' calcium activity

Ex vivo, we observed a specific response 20 min after bath application of PRL, similar in both sexes (Figure 7A and Table S6 for control experiments). PRL application did not induce recruitment of cells (n of active cells, Table S6), but a clear spatiotemporal reorganization of the calcium activity appeared, dominated by long periods of coactivity compared to control conditions with a shift of I_{eff} toward the subgroup of maximum efficiency (Figure 7B).[16,17]

This organization was characterized by a modification of the topological feature of the network with an increase in the proportion of cells presenting a high degree of cross-correlation (CC > 0.6) (with % of cells presenting CC > 0.6 = 11.46 ± 4.78% in control vs. 26.6 ± 3.9% after PRL (Student's two-tailed t-test for paired data $p = 0.0003$, $n = 8$), reflecting an increase in temporal synchronization between TIDA neurons (Figure 7C Top and Table S6). In addition, the topology factor: modularity (M), which measures the strength of division of a network into groups, is significantly decreased by PRL application, with M = 0.55 ± 0.07 in control vs. 0.27 ± 0.05 after PRL (Student's two-tailed t-test for paired data, $p = 0.012$, $n = 8$) (Figure 7C bottom right).

PRL induced an increase in the length of synchronized calcium events (increased n of long events cells (from 6.2 ± 2 cells to 38 ± 7.8 cells (post-hoc Sidak test, $p = 0.0041$ [$n = 12$]) (Figure 7D, left and Table S6), and duration of Ens (from 0.68 ± 0.11 s to 2.3 ± 0.52 s (post-hoc Sidak test, $p = 0.0029$ [$n = 12$]) (Figure 7D, right and Table S6). Examples of recordings for female PRL responses are presented in supplementary data (see Video S4).

High synchronization of TIDA neurons' calcium activity occurred spontaneously *in vivo* and corresponded to the highest efficiency in inhibiting $[PRL]_{blood}$

In vivo, we observed some episodes of such peculiar organization occurring spontaneously (males $n = 4$, females $n = 1$) (Figure 7E, Video S4).

These recordings all belong to I_{eff} maximum efficiency and are associated with the lower levels of $[PRL]_{blood}$ (2.56 ± 0.39 ng/mL [$n = 5$] vs. 4.59 ± 0.54 ng/mL [$n = 10$], Student's t test, $p = 0.03$) (Figure 7F and Table S7). High synchronization was discriminated from other Max efficiency recordings by transitivity (T > 0.8) (T = 0.9 ± 0.04 [$n = 5$] compared to T = 0.6 ± 0.03 [$n = 12$] for Max efficiency; (Student's two-tailed t-test for unpaired data, $p = 0.04$). (Figure 7G Top).

We compared the high synchronization recording characteristics with the rest of the maximum efficiency recordings. High synchronization recordings featured an increase in the percentage of cells presenting CC > 0.6 (CC > 0.6 = 37.81 ± 12.38% ($n = 5$) vs. 10.7 ± 2.3% ($n = 12$) (Student's two-tailed t-test for unpaired data, $p = 0,0057$) (Figure 7G, bottom left), resulting from a shift toward a higher cross correlation between TIDA neurons. Modularity (M) is significantly decreased in high synchronization with M = 0.15 ± 0.09 ($n = 5$) s 0.36 ± 0.05 ($n = 12$) (student's two-tailed t-test for unpaired data, $p = 0.036$) (Figure 7G, bottom right).

High synchronization recordings showed significant increases in n of long cells (20.8 ± 10.8 cells ($n = 5$) vs. 5.92 ± 0.98 cells ($n = 12$); (Student's two-tailed t-test for unpaired data $p = 0.04$) and in N cells per Ens cells (9.7 cells ± 2.59 ($n = 5$) vs. 3.57 ± 0.33 ($n = 12$); (Student's two-tailed t-test for unpaired data $p = 0.0022$) (Figure 7H).

Examples of recordings for males in maximum efficiency and high synchronization configuration are presented in the supplemental information (see Videos S2 and S5).

One male was recorded longitudinally over 40 min (Figure 7I). It displayed spontaneous high synchronization activity in the first phase of recording, and this activity was associated with low levels of PRL. We observed a transition from high synchronization to no efficiency organization associated with an increase in $[PRL]_{blood}$ after 10 min, followed by a decrease in $[PRL]_{blood}$ associated with a transition to low efficiency. Modulation of TIDA neurons efficiency may, therefore, parallel quick changes in $[PRL]_{blood}$ at the timescale of minutes.

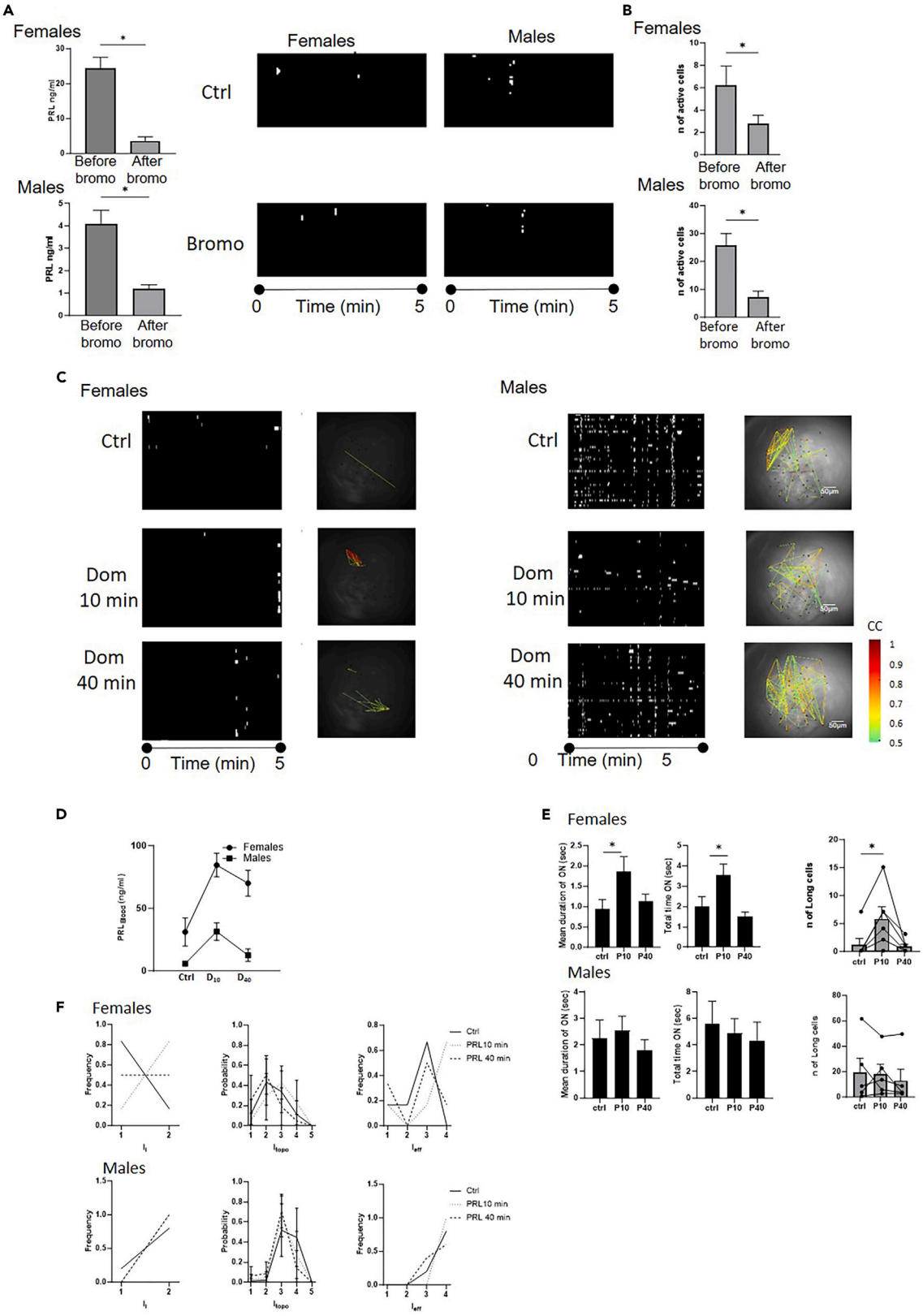
A
Females
PRL ng/ml
Before bromo
After bromo
Males
Ctrl
Bromo
Females
Males
0
Time (min)
5
B
Females
n of active cells
Before bromo
After bromo
Males
C
Females
Ctrl
Dom 10 min
Dom 40 min
Males
CC
D
Females
Males
Ctrl
E
Females
Mean duration of ON (sec)
Total time ON (sec)
n of Long cells
ctrl
P10
P40
Males
F
Females
Frequency
Probability
PRL10 min
PRL 40 min
Males

Figure 6. Modulation of $[PRL]_{blood}$ affects both male and female TIDA activity

(A) $[PRL]_{blood}$ in females (top left) and males (bottom left) before and after Bromocriptine treatment *in vivo*. For female and male experiments groups were equal ($n = 3$). Representative images of on/off raster-plots (right) before Bromocriptine injections and 24 h after second injection for both males and females (B) N of active cells was significantly decreased in both females (top) and males' group (bottom).

(C) Representative images of on/off raster-plots, coactivity plots and cross-correlation functional networks for females (Left 3 panels) and males (Right 3 panels), before, 10 and 40 min after Domperidone injection (D) Changes in $[PRL]_{blood}$ after 10 and 40 min after Domperidone injection for females ($n = 6$) and males ($n = 6$) (E) From left to right—Mean duration of ON event, Total time in ON event, number of cells presenting Long events for Females ($n = 6$) (Top) and Males ($n = 6$) Bottom.

(F) CLM of $I_{L.}$, I_{topo}, I_{coact}, and I_{eff} did not show difference between groups. For correlation analysis Pearson coefficient. CLM model used for indexes as categorical data. *$p < 0.05$, **$p < 0.01$, ***$p < 0.001$, ****$p < 0.00001$. One-way ANOVA for depended variables used for comparisons of 3 groups. Sidak-test for multiply comparisons is used if ANOVA reveal differences. CLM model used for indexes as categorical data. *$p < 0.05$.

DISCUSSION

TIDA neurons organize as a functional network with scalable efficiency matching $[PRL]_{blood}$

This work sheds light on the sex-independent dynamic nature of the TIDA neurons network *in vivo*, allowing $[PRL]_{blood}$ homeostasis to be maintained. It has been shown that DA secreted by TIDA neurons represses PRL secretion by pituitary lactotroph cells that otherwise tend to secrete continuously, so the more efficiently TIDA neurons secrete DA, the lower $[PRL]_{blood}$ is.[20] In our study, we found that TIDA neurons' ability to inhibit PRL secretion is determined by two main factors, the length of calcium events and their ability to form plastic economic networks.

In vivo, the temporal organization of spontaneous calcium activity in single TIDA neurons varies over time, displaying a variety of patterns similar to those reported *ex vivo*,[13,20] allowing TIDA neurons to organize into a diversity of functional networks of different theoretical efficiency. The degree and temporal weight of synchronization between cells (neuronal coherence or phase-locking) and the capacity to generate slow oscillating synchronized calcium waves have been reported to be hallmarks of efficiency in numerous neuroendocrine and neuronal populations.[21–23] This slow synchronization within the neuroendocrine systems contributes to a pulsatile pattern in the release of hormones. This pulsatility is critical for achieving precise and controlled physiological responses in neuroendocrine systems.[24,25]

Within neurons, short $[Ca^{2+}]_i$ transients' duration (<1 s) (evoked by synaptic activation) are best characterized.[26] They coexist with slower transients resulting from intracellular stores calcium release.[27,28] These slower $[Ca^{2+}]_i$ transients are characteristic of several neuroendocrine systems. The GnRH neurons and Kisseptin neurons of the arcuate, controlling pituitary luteinizing hormone (LH), perfectly illustrate neuroendocrine long (10–15 s), slow synchronized oscillations.[29,30]

I_{eff} offers a complete tool combining single-cell calcium activity characteristics (I_l), strength of the networking, and weight of synchronization (I_{topo} and I_{coact}), to evaluate the efficiency of the TIDA neurons network.

In TIDA neurons, the main factor influencing I_{eff} was the number of cells presenting long events (I_l). Recordings presenting more than one cell with long events were all classified as having medium or maximum efficiency, with the typology and index of coactivity providing a subgradient of increasing efficiency in inhibiting PRL secretion.

The presence of a single long event cell is not sufficient for the TIDA network to belong to optimal efficiency networking. Furthermore, it requires specific topological organization into networks of increasing efficiency (regular, random, and small world configurations).[31,32–34] Due to efficient topology, even without long event cells, efficiency can still reach medium efficiency.

The configuration of maximal efficiency is composed of dense local connections mediating a short path length between any pair of neurons in the network.[20,31] This small-world configuration minimizes wiring costs,[21] thus maximizing information processing efficiency.[22] In this configuration, the population is divided into localized modules, composed of densely interconnected nodes. This compartmentalization of function enhancing robustness and flexibility confers an important adaptive advantage.[23] The level of coactivity provides a second subgradient of efficiency. High temporal weight of coactivity ($I_{coact} \geq 2$) is characteristic of medium and maximum efficient network, recordings with a high number of cells involved in a coactive episode ($I_{coact} \geq 3$) correspond to maximum efficiency network.

While I_{coact} effectively reports the weight of coactive neurons, it is a weak indicator for the overall synchronization of the neuronal population. The use of cross-correlation between cell analyses resolved the issue of alignment of the signal (i.e., synchronization of the calcium activity). Both *in vivo* (spontaneously) and *ex vivo* (after PRL application), we observed a subgroup of maximum efficiency recording, characterized by slow and highly synchronized long waves of calcium, separated by periods of silence, providing a visual pop-corning effect. Neurons became active only in a synchronous manner. This high synchronization (HS) group presents high transitivity ($T > 0.8$). Transitivity reflects the relations between neurons, which are sets of ordered pairs that relate elements from one set of elements to another. High transitivity therefore corresponds to a high degree of mutual relation between neurons that can be reached by high synchronization. This activity may represent the best configuration of maximum efficiency as it was associated with the lowest levels of $[PRL]_{blood}$. In this configuration, we observed, both in and *ex vivo*, a decrease in modularity. This marker measures the propensity of the neurons to form subgroups of active cells. This decrease reflects the fact that under high synchronization, TIDA neurons coactivate as large ensembles (illustrated by the increase in the number of cells per ensemble), tending to form a single coactive ensemble of the whole recorded population.

This type of coordinated activity matches our previous work on DA secretion at the level of ME,[13] where low TIDA neuron oscillations (0.2 hz) sustain DA release.[16,17] It advocates for the existence of a highly efficient plastic network within the TIDA neurons that can be recruited under physiological demand. We suggest that the spontaneous, highly synchronized activity is the response to an undetected spontaneous increase in $[PRL]_{blood}$ and corresponds to the adaptation of the TIDA neurons network to PRL feedback. TIDA neurons displayed, in both

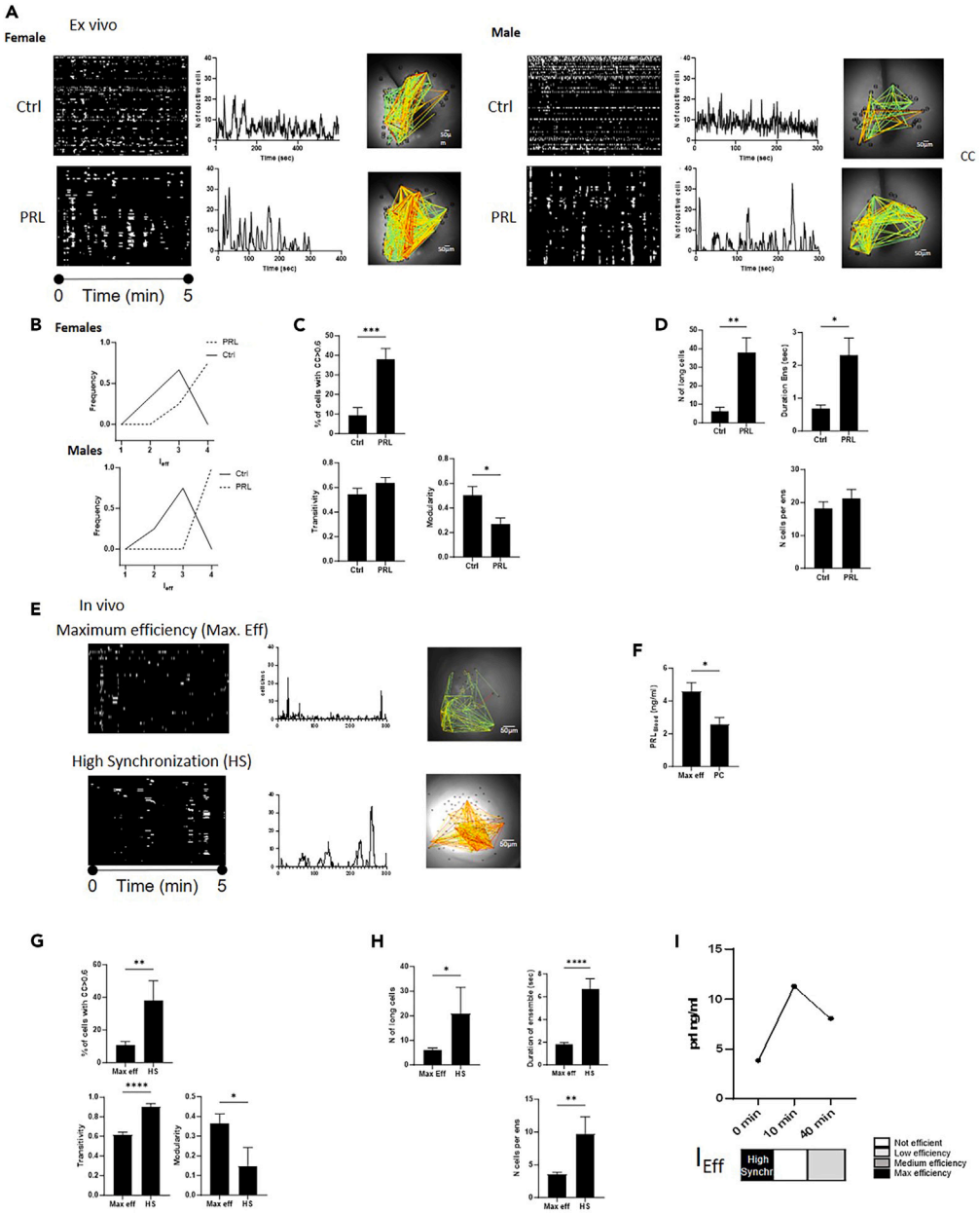

Figure 7. Highly synchronized networking (SN) as an energy-efficient subtype of Maximum efficiency (ME) activity of TIDA

(A) Effect of PRL application *ex vivo*. Representative image of on/off raster-plots (Left), coactivity plots (Center) and cross-correlation functional networks (Right) for control and after PRL application in females (Left) and males (Right) (B) Frequency distribution of the recordings in different I_{eff} shows shift toward Max Efficiency sub-group after PRL application in both females (Top) and males (Bottom).

(C) PRL induces modification of the topology after PRL application. The percentage of cells presenting high degree of cross-correlation (CC > 0.6) (Top) is increased after PRL application. Transitivity is unchanged (Bottom Left). Modularity is significantly reduced (Bottom Right) (Pooled females and Males $n = 12$).

(D) Number of cells presenting Long events (Top Left), Duration of Ens (Top Right) are significantly increased after PRL application. Number of cells per Ens is unchanged (Bottom right).

(E) Representative images of on/off raster-plots (Left), coactivity plots (Center) and cross-correlation functional networks (Right) for simple maximum efficiency activity (Top) and high synchronization (Bottom) *in vivo* (F) Average levels of prolactin in blood in maximum efficiency (Max Eff.) and high synchronization (HS) groups *in vivo*.

(G) The percentage of cells presenting high degree of cross-correlation (CC > 0.6) (Top) and Transitivity (Bottom Left) are increased in highly synchronized compared to other Max efficiency recordings. Modularity is significantly reduced (Bottom Right).

Figure 7. *Continued*

(H) Number of cells presenting long events (Top Left), duration of Ens (Top Right) and number of cells per Ens (Bottom right) are significantly increased in highly synchronized recordings.

(I) Example of 1-h longitudinal study demonstrating antiparallel modifications of efficiency of TIDA activity and prolactin blood levels in male. Student unpaired two-tailed t test used for comparison of 2 groups. CLM model used for indexes as categorical data. *$p < 0.05$, **$p < 0.01$, ***$p < 0.001$, ****$p < 0.00001$.

sexes, intrinsic wiring allowing them to organize their activity and modulate their efficiency to inhibit PRL secretion ranging from low to highly efficient depending on the physiological context. They can even reach the highest efficiency topology of small world configuration, *ex vivo*, under PRL activation and spontaneously, *in vivo*, corresponding to the lowest $[PRL]_{blood}$. By combining (I_I I_{topo} and I_{coact}), we provided an index of efficiency (I_{eff}), highly reliable in predicting $[PRL]_{blood}$.

The ability to organize as a network is an intrinsic property of TIDA neurons as the whole range of I_{eff} was observed *ex vivo*. The size of the recording window *in vivo* (i.e., the diameter of the GRIN lens) restrains our analysis to a fraction of the TIDA neuron population, allowing us to detect a 2D network. In the whole arcuate, TIDA neurons probably organize as a plastic 3D network able to modulate, in time, the $[PRL]_{blood}$ according to the physiological demand. The switch between different states of efficiency can occur in a short time frame (5–10 min) (as shown in longitudinal following males) or organize over days (longitudinal study of the estrous cycle), modulating both short- and long-term $[PRL]_{blood}$ changes, suggesting that this organization may represent the canonical mechanism for controlling $[PRL]_{blood}$ *in vivo*. Hence, we propose that TIDA neurons function as neuronal Hebbian ensembles,[18] presenting stereotyped functional organization adapted to physiological demands in both sexes.

The plasticity of networking efficiency allows both short-term (ultradian) and long-term modulation of $[PRL]_{blood}$

During the estrous cycle, I_{eff} reflects long-term $[PRL]_{blood}$ modifications. Despite the importance of mouse models in research, the precise temporal levels of circulating gonadal steroids and hormones across the estrous cycle remain poorly described, and our knowledge often comes from the rat.[19] Unfortunately, the profiles of secretion are very different between these species, which can induce errors in data interpretation. We confirm previous results in mice showing that PRL was elevated during diestrus compared to estrus, without any defined surge during the estrous cycle.[19,35]

The factors involved in the organization and synchronization of the networks are still unknown. *Ex vivo*, harmonized electrical activity between TIDA neurons had been reported in both rats[15] and mice.[12] It was due, in rats, to gap junctional coupling and induced synchronization of oscillating bursting cells,[15] but this was absent in mice[12] which displayed a weaker correlation between TIDA neurons' electrical activity, corresponding to a loose harmonization of the activity. This type of networking in acute brain slice was sufficient to correlate with DA secretion at the ME level, measured by real-time amperometry.[12]

Several neuromodulators and neurotransmitters are able to influence TIDA neurons. TIDA neurons express somatic D2 DA auto-receptor, adjusting oscillation, *ex vivo*, via a fast autofeedback of DA.[31] The role of DA in modulating networking *in vivo* needs to be tested using, for example, a mouse model of time controlled specific loss of function of D2 receptors.[20]

PRL is known as a primary modulator of its own secretion through activation of TIDA neurons. We and others described the effect of PRL *ex vivo*, both on electrical and calcium activity.[12,14] Here, we show that PRL very effectively induced a switch of the networking toward Max efficiency *ex vivo*. *In vivo*, experimental increase of $[PRL]_{blood}$ (oPRL or domperidone injection), induced a response significant only in females, with a characteristic increase in N of long events cells. In females after PRL, I_{eff}, reaches the value observed in males during control. It reflected the fact that TIDA neurons in males were already in highly activated mode in basal conditions, probably close to their maximum activation state (Max I_{eff}). The amounts of injected PRL in our experiments may be not sufficient to induce any detectable additional short-term activation.

The switch from one state of efficiency to another may be influenced by sexual hormone changes. Estradiol has been shown to contribute indirectly to TIDA neurons control by modulating PRL gene transcription[21] and subsequent PRL feedback on them. It may also modulate their excitability by acting on ionic channels, as described in the hypothalamus.[22,23] Modification of the levels of estradiol could therefore account for the difference in TIDA neurons activity during the estrous cycle, participating in the adaptation of the $[PRL]_{blood}$ to the physiological demand. As for testosterone, it inhibits basal activation of TIDA neurons in rats.[24] The dynamic of the balance between the hormones in the two sexes could be at the root of the modification of TIDA neurons efficiency.

The sex-specific number of active TIDA contributes to the $[PRL_{blood}]$ sexual dimorphism

Despite differences in their physiology, TIDA neurons did not appear anatomically different between sexes.[25] Our *ex vivo* results confirm that TIDA neurons are not intrinsically sexually dimorphic. Disconnected from *in vivo* extrinsic factors, the majority of TIDA neurons were spontaneously active, connected to form efficient networks, and responded to PRL application similarly in both sexes. In contrast, TIDA neuron functional activity was highly sexually different *in vivo*. The main feature of this difference was the proportion of spontaneously active cells, with very low numbers in females. These numbers were not significantly modified, either spontaneously, or after PRL application, suggesting that, *in vivo*, the proportion of functional TIDA neurons is fixed and independent of the physiological state. Interestingly, the number of spontaneously active cells *in vivo* differed from *ex vivo*, with females *in vivo* showing fewer active cells than we extrapolated from *ex vivo* recordings, while males showed a higher number of active cells. This suggests that extrinsic factors may modulate *in vivo* TIDA neurons differently depending on the sex, leading to functional inhibition in females and activation in males.

If our decoding of the control of $[PRL]_{blood}$. by TIDA neurons is appropriate for virgin animals of both sexes, how the network adapts to the specific physiological stage of gestation and lactation in females remains unclear. During these periods, $[PRL]_{blood}$. displays a very specific temporal pattern of secretion, from a semi-circadian rhythm during the first half of pregnancy to a drastic decrease in secretion during the second half, and finally, a chronic hyperprolactinemia with superimposed transient increase of $[PRL_{blood}.]$ when pups are suckling during lactation. We previously showed, *ex vivo*, that basal and PRL-induced electrical activity characteristics of TIDA neurons were not modified during lactation,[12] but that their ability to secrete DA was modified both *ex* and *in vivo*[12,13] due to a decrease in DA production to the benefit of enkephalin.[26,27] *Ex vivo*, in rats, oxytocin (OT) modified the electrical activity pattern of the TIDA neurons during lactation.[28] The pattern of TIDA neurons activity *in vivo* during lactation is still unknown. The interaction of both high PRL and OT with TIDA neurons may participate in a lactation-specific pattern of secretion that needs to be explored.

Our results suggest that PRL may play a part in controlling the number of active cells. In fact, the condition of chronic low PRL (bromocriptine treatment), was the only situation where we observed a modification in the number of active cells. In males, bromocriptine induced a drastic drop of $[PRL]_{blood}$ outside the homeostatic physiological range. In this condition, the number of active cells was significantly reduced in both males and females. This suggests that $[PRL]_{blood}$ in the physiological range is necessary for an appropriate number of TIDA neurons to activate *in vivo*. Under a certain threshold, corresponding to the lower limit of the physiological range, the system we described with a fixed number of active cells and modulation of its networking properties is not valid anymore.

The other possible modulators are not yet identified. Sexually dimorphic circulating factors, sex specific sensitivity to them, and/or sexually dimorphic wiring of TIDA neurons with another part of the brain [25,29,30,32–34,36], could be at the origin of this difference between sexes.

This difference between sexes in the spontaneous activity of TIDA neurons *in vivo* suggests that the physiological environment plays a crucial role in regulating the functional properties of these neurons, and highlights the importance of studying neural circuits in their native context. Recognizing the sexual dimorphism of PRL secretion and its modulation could be of major importance in the management of the numerous disorders involving PRL secretion dysregulation. As in the case of hyperprolactinemia, dopaminergic agonists are the first line of treatment, our study, which provides a better understanding of the sex-specific relationship between PRL secretion and DA secreted by TIDA neurons, also stresses the importance of a sex-specific management of these pathologies.

Limitations of the study

This *in vivo* study was conducted using fixed stereotaxic coordinates and large Grin lenses (500μm diameter). The difference in functionality of TIDA neurons depending on their precise anatomical localization in the arcuate nucleus (anteroposterior and dorsoventral), would require the use of a smaller Grin lens and definition of systematic implantation coordinates covering the different anatomical compartments. The use of freely moving (miniscopes) instead of head-fixed set-up would also provide valuable improvement in understanding *in vivo* TIDA neurons functionality.

STAR★METHODS

Detailed methods are provided in the online version of this paper and include the following:

- KEY RESOURCES TABLE
- RESOURCE AVAILABILITY
  - Lead contact
  - Materials availability
  - Data and code availability
- EXPERIMENTAL MODEL AND STUDY PARTICIPANT DETAILS
  - Mice
- METHOD DETAILS
  - Brain slice preparation
  - *Ex vivo* calcium imaging
  - Stereotaxic surgery
  - *In vivo* calcium imaging
  - Perfusion-fixation and verification of GRIN lens position
  - Ultrasensitive PRL ELISA
- QUANTIFICATION AND STATISTICAL ANALYSIS
  - Calcium imaging data processing
  - Coactive and functional networks analysis
  - Statistical analysis

SUPPLEMENTAL INFORMATION

Supplemental information can be found online at https://doi.org/10.1016/j.isci.2024.109876.

ACKNOWLEDGMENTS

This work was supported by grant from Agence Nationale de la Recherche (ANR-18-CE92-0010, France-BioImaging ANR-10-INBS-04, ANR-18-CE14-0017, ANR-22-CE14-0001-01).

AUTHOR CONTRIBUTIONS

S.C, conceptualization, investigation, methodology, writing – original draft, supervision; L.H. investigation, methodology and software; P.F. methodology and software; A.G. investigation and methodology; E.G. investigation and methodology; P.C. investigation and methodology; P.M. conceptualization, supervision; A.O.M. conceptualization, methodology, writing – original draft, project administration, and funding acquisition.

DECLARATION OF INTERESTS

The authors declare no competing interests.

Received: October 6, 2023
Revised: February 9, 2024
Accepted: April 29, 2024
Published: May 3, 2024

REFERENCES

1. Guillou, A., Romanò, N., Steyn, F., Abitbol, K., Le Tissier, P., Bonnefont, X., Chen, C., Mollard, P., and Martin, A.O. (2015). Assessment of lactotroph axis functionality in mice: longitudinal monitoring of PRL secretion by ultrasensitive-ELISA. Endocrinology *156*, 1924–1930.
2. Corona, G., Rastrelli, G., Bianchi, N., Sparano, C., Sforza, A., Vignozzi, L., and Maggi, M. (2023). Hyperprolactinemia and male sexual function: focus on erectile dysfunction and sexual desire. Int. J. Impot. Res. https://doi.org/10.1038/s41443-023-00717-1.
3. Bernard, V., Young, J., and Binart, N. (2019). Prolactin - a pleiotropic factor in health and disease. Nat. Rev. Endocrinol. *15*, 356–365.
4. Bjorklund, A., Moore, R.Y., Nobin, A., and Stenevi, U. (1973). The organization of tubero-hypophyseal and reticulo-infundibular catecholamine neuron systems in the rat brain. Brain Res. *51*, 171–191.
5. Reymond, M.J., and Porter, J.C. (1985). Involvement of hypothalamic dopamine in the regulation of prolactin secretion. Horm. Res. *22*, 142–152.
6. Kokay, I.C., and Grattan, D.R. (2005). Expression of mRNA for prolactin receptor (long form) in dopamine and pro-opiomelanocortin neurones in the arcuate nucleus of non-pregnant and lactating rats. J. Neuroendocrinol. *17*, 827–835.
7. Lerant, A.A., DeMaria, J.E., and Freeman, M.E. (2001). Decreased expression of fos-related antigens (FRAs) in the hypothalamic dopaminergic neurons after immunoneutralization of endogenous prolactin. Endocrine *16*, 181–187.
8. Ben-Jonathan, N. (1985). Dopamine: a prolactin-inhibiting hormone. Endocr. Rev. *6*, 564–589.
9. MacLeod, R.M., Fontham, E.H., and Lehmeyer, J.E. (1970). Prolactin and growth hormone production as influenced by catecholamines and agents that affect brain catecholamines. Neuroendocrinology *6*, 283–294.
10. Wang, H.J., Hoffman, G.E., and Smith, M.S. (1993). Suppressed tyrosine hydroxylase gene expression in the tuberoinfundibular dopaminergic system during lactation. Endocrinology *133*, 1657–1663.
11. Trocme, C., Sarkis, C., Hermel, J.M., Duchateau, R., Harrison, S., Simonneau, M., Al-Shawi, R., and Mallet, J. (1998). CRE and TRE sequences of the rat tyrosine hydroxylase promoter are required for TH basal expression in adult mice but not in the embryo. Eur. J. Neurosci. *10*, 508–521.
12. Romano, N., Yip, S.H., Hodson, D.J., Guillou, A., Parnaudeau, S., Kirk, S., Tronche, F., Bonnefont, X., Le Tissier, P., Bunn, S.J., et al. (2013). Plasticity of hypothalamic dopamine neurons during lactation results in dissociation of electrical activity and release. J. Neurosci. *33*, 4424–4433.
13. Romano, N., Guillou, A., Hodson, D.J., Martin, A.O., and Mollard, P. (2017). Multiple-scale neuroendocrine signals connect brain and pituitary hormone rhythms. Proc. Natl. Acad. Sci. USA *114*, 2379–2382.
14. Lyons, D.J., Hellysaz, A., and Broberger, C. (2012). Prolactin regulates tuberoinfundibular dopamine neuron discharge pattern: novel feedback control mechanisms in the lactotrophic axis. J. Neurosci. *32*, 8074–8083.
15. Lyons, D.J., Horjales-Araujo, E., and Broberger, C. (2010). Synchronized network oscillations in rat tuberoinfundibular dopamine neurons: switch to tonic discharge by thyrotropin-releasing hormone. Neuron *65*, 217–229.
16. Stagkourakis, S., Smiley, K.O., Williams, P., Kakadellis, S., Ziegler, K., Bakker, J., Brown, R.S.E., Harkany, T., Grattan, D.R., and Broberger, C. (2020). A Neuro-hormonal Circuit for Paternal Behavior Controlled by a Hypothalamic Network Oscillation. Cell *182*, 960–975.e15.
17. Lyons, D.J., and Broberger, C. (2014). TIDAL WAVES: Network mechanisms in the neuroendocrine control of prolactin release. Front. Neuroendocrinol. *35*, 420–438.
18. Morris, R.G., and Hebb, D.O. (1999). The Organization of Behavior, Wiley: New York; 1949. Brain Res. Bull. *50*, 437.
19. Wall, E.G., Desai, R., Khant Aung, Z., Yeo, S.H., Grattan, D.R., Handelsman, D.J., and Herbison, A.E. (2023). Unexpected Plasma Gonadal Steroid and Prolactin Levels Across the Mouse Estrous Cycle. Endocrinology *164*, bqad070.
20. Puighermanal, E., Biever, A., Espallergues, J., Gangarossa, G., De Bundel, D., and Valjent, E. (2015). drd2-cre:ribotag mouse line unravels the possible diversity of dopamine d2 receptor-expressing cells of the dorsal mouse hippocampus. Hippocampus *25*, 858–875.
21. Shull, J.D., and Gorski, J. (1989). Estrogen regulation of prolactin gene transcription *in vivo*: paradoxical effects of 17 beta-estradiol dose. Endocrinology *124*, 279–285.
22. Pan, J.T., Kow, L.M., and Pfaff, D.W. (1986). Single-unit activity of hypothalamic arcuate neurons in brain tissue slices. Effects of anterior pituitary hormones, cholecystokinin-octapeptide, and neurotransmitters. Neuroendocrinology *43*, 189–196.
23. Bosch, M.A., Kelly, M.J., and Rønnekleiv, O.K. (2002). Distribution, neuronal colocalization, and 17beta-E2 modulation of small conductance calcium-activated K(+) channel (SK3) mRNA in the guinea pig brain. Endocrinology *143*, 1097–1107.
24. Toney, T.W., Lookingland, K.J., and Moore, K.E. (1991). Role of testosterone in the regulation of tuberoinfundibular dopaminergic neurons in the male rat. Neuroendocrinology *54*, 23–29.
25. Ciofi, P., Leroy, D., and Tramu, G. (2006). Sexual dimorphism in the organization of the rat hypothalamic infundibular area. Neuroscience *141*, 1731–1745.
26. Yip, S.H., Romanò, N., Gustafson, P., Hodson, D.J., Williams, E.J., Kokay, I.C., Martin, A.O., Mollard, P., Grattan, D.R., and Bunn, S.J. (2019). Elevated Prolactin during Pregnancy Drives a Phenotypic Switch in Mouse Hypothalamic Dopaminergic Neurons. Cell Rep. *26*, 1787–1799.e5.
27. Le Tissier, P.R., Hodson, D.J., Martin, A.O., Romanò, N., and Mollard, P. (2015). Plasticity of the prolactin (PRL) axis: mechanisms underlying regulation of output in female mice. Adv. Exp. Med. Biol. *846*, 139–162.
28. Briffaud, V., Williams, P., Courty, J., and Broberger, C. (2015). Excitation of tuberoinfundibular dopamine neurons by

oxytocin: crosstalk in the control of lactation. J. Neurosci. *35*, 4229–4237.
29. De Seranno, S., Estrella, C., Loyens, A., Cornea, A., Ojeda, S.R., Beauvillain, J.C., and Prevot, V. (2004). Vascular endothelial cells promote acute plasticity in ependymoglial cells of the neuroendocrine brain. J. Neurosci. *24*, 10353–10363.
30. Durham, R.A., Johnson, J.D., Moore, K.E., and Lookingland, K.J. (1996). Evidence that D2 receptor-mediated activation of hypothalamic tuberoinfundibular dopaminergic neurons in the male rat occurs via inhibition of tonically active afferent dynorphinergic neurons. Brain Res. *732*, 113–120.
31. Stagkourakis, S., Kim, H., Lyons, D.J., and Broberger, C. (2016). Dopamine Autoreceptor Regulation of a Hypothalamic Dopaminergic Network. Cell Rep. *15*, 735–747.
32. Kannangara, H., Cullen, L., Miyashita, S., Korkmaz, F., Macdonald, A., Gumerova, A., Witztum, R., Moldavski, O., Sims, S., Burgess, J., et al. (2023). Emerging roles of brain tanycytes in regulating blood-hypothalamus barrier plasticity and energy homeostasis. Ann. N. Y. Acad. Sci. *1525*, 61–69.
33. Miyata, S. (2022). Glial functions in the blood-brain communication at the circumventricular organs. Front. Neurosci. *16*, 991779.
34. Ribeiro, A.B., Leite, C.M., Kalil, B., Franci, C.R., Anselmo-Franci, J.A., and Szawka, R.E. (2015). Kisspeptin regulates tuberoinfundibular dopaminergic neurones and prolactin secretion in an oestradiol-dependent manner in male and female rats. J. Neuroendocrinol. *27*, 88–99.
35. Phillipps, H.R., Khant Aung, Z., and Grattan, D.R. (2022). Elevated prolactin secretion during proestrus in mice: Absence of a defined surge. J. Neuroendocrinol. *34*, e13129.
36. Wagner, E.J., Moore, K.E., and Lookingland, K.J. (1993). Sexual differences in N-methyl-D-aspartate receptor-mediated regulation of tuberoinfundibular dopaminergic neurons in the rat. Brain Res. *611*, 139–146.
37. Turiault, M.P.S., Milet, A., Parlato, R., Rouzeau, J.D., Lazar, M., and Tronche, F. (2007). Analysis of dopamine transporter gene expression pattern—generation of DAT-iCre transgenic mice. FEBS J. *274*, 3568–3577.
38. Liutkus, A. (2015). Scale-Space Peak Picking. HAL.
39. Smedler, E., Malmersjö, S., and Uhlén, P. (2014). Network analysis of time-lapse microscopy recordings. Front. Neural Circ. *8*, 111.
40. Rubinov, M., and Sporns, O. (2010). Complex network measures of brain connectivity: uses and interpretations. Neuroimage *52*, 1059–1069.
41. Mourao, M., Satin, L., and Schnell, S. (2014). Optimal experimental design to estimate statistically significant periods of oscillations in time course data. PLoS One *9*, e93826.
42. Lee, M.D., Buckley, C., Zhang, X., Louhivuori, L., Uhlén, P., Wilson, C., and McCarron, J.G. (2022). Small-world connectivity dictates collective endothelial cell signaling. Proc. Natl. Acad. Sci. USA *119*. e2118927119.
43. Madisen, L., Garner, A.R., Shimaoka, D., Chuong, A.S., Klapoetke, N.C., Li, L., van der Bourg, A., Niino, Y., Egolf, L., Monetti, C., et al. (2015). Transgenic mice for intersectional targeting of neural sensors and effectors with high specificity and performance. Neuron *85*, 942–958.
44. Ajayi, A.F., and Akhigbe, R.E. (2020). Staging of the estrous cycle and induction of estrus in experimental rodents: an update. Fertil. Res. Pract. *6*, 5.
45. Romanò, N.Y.S., Hodson, D.J., Guillou, A., Parnaudeau, S., Kirk, S., Tronche, F., Bonnefont, X., Le Tissier, P., Bunn, S.J., Grattan, D.R., et al. (2013). Plasticity of Hypothalamic Dopamine Neurons during Lactation Results in Dissociation of Electrical Activity and Release. J. Neurosci. *33*, 4424–4433.
46. Zhang, L., Liang, B., Barbera, G., Hawes, S., Zhang, Y., Stump, K., Baum, I., Yang, Y., Li, Y., and Lin, D.T. (2019). Miniscope GRIN Lens System for Calcium Imaging of Neuronal Activity from Deep Brain Structures in Behaving Animals. Curr. Protoc. Neurosci. *86*, e56.
47. Zhang, X., and van den Pol, A.N. (2015). Dopamine/Tyrosine Hydroxylase Neurons of the Hypothalamic Arcuate Nucleus Release GABA, Communicate with Dopaminergic and Other Arcuate Neurons, and Respond to Dynorphin, Met-Enkephalin, and Oxytocin. J. Neurosci. *35*, 14966–14982.
48. Barone, J.A. (1999). Domperidone: a peripherally acting dopamine2-receptor antagonist. Ann. Pharmacother. *33*, 429–440.
49. Sanger, G.J., and Andrews, P.L.R. (2018). A History of Drug Discovery for Treatment of Nausea and Vomiting and the Implications for Future Research. Front. Pharmacol. *9*, 913.
50. Pnevmatikakis, E.A., and Giovannucci, A. (2017). NoRMCorre: An online algorithm for piecewise rigid motion correction of calcium imaging data. J. Neurosci. Methods *291*, 83–94.
51. Chen, T.W., Wardill, T.J., Sun, Y., Pulver, S.R., Renninger, S.L., Baohan, A., Schreiter, E.R., Kerr, R.A., Orger, M.B., Jayaraman, V., et al. (2013). Ultrasensitive fluorescent proteins for imaging neuronal activity. Nature *499*, 295–300.
52. Xing, X., and Wu, C.F. (2018). Unraveling Synaptic GCaMP Signals: Differential Excitability and Clearance Mechanisms Underlying Distinct Ca(2+) Dynamics in Tonic and Phasic Excitatory, and Aminergic Modulatory Motor Terminals in Drosophila. eNeuro *5*, ENEURO.0362-17.2018.
53. Uhlen, P. (2004). Spectral analysis of calcium oscillations. Sci. STKE *2004*, pl15.
54. Miller, J.e.K., Ayzenshtat, I., Carrillo-Reid, L., and Yuste, R. (2014). Visual stimuli recruit intrinsically generated cortical ensembles. Proc. Natl. Acad. Sci. USA *111*, E4053–E4061.
55. Latora, V., and Marchiori, M. (2001). Efficient behavior of small-world networks. Phys. Rev. Lett. *87*, 198701.
56. Achard, S., and Bullmore, E. (2007). Efficiency and cost of economical brain functional networks. PLoS Comput. Biol. *3*, e17.
57. Girvan, M., and Newman, M.E.J. (2002). Community structure in social and biological networks. Proc. Natl. Acad. Sci. USA *99*, 7821–7826.

STAR★METHODS

KEY RESOURCES TABLE

REAGENT or RESOURCE	SOURCE	IDENTIFIER
Antibodies		
Guinea Pig Anti-Mouse Prolactin	NIDDK-NHPP	AFP65191; RRID:AB_2756841
Rabbit anti-mouse PRL	Parlow National Hormone and Peptide Program	AFP107120402; RRID:AB_2721133
Donkey Anti-Rabbit IgG, Whole Ab ECL Antibody, HRP Conjugated	Fisher Scientific	NA934; RRID:AB_772206
Chemicals, peptides, and recombinant proteins		
Human recombinant Prolactin	Sigma-Aldrich	SRP9000
Domperidone	Abcam	ab147491
Bromocriptine mesylate	Tocris	Cat. No. 0427
Recombinant mouse PRL	NIDDK-NHPP	AFP-405C
O-phenylenediamine	Life technologies	SAS 00-2003
Experimental models: Organisms/strains		
DAT-iCRE- GCAMP6f	Turiault et al.[37]	JAX stock 024105
Software and algorithms		
MetaMorph	Molecular Devices	https://support.moleculardevices.com/s/article/MetaMorph-Software-Suite-Knowledge-Base
Non-Rigid Motion Correction (NoRMCorre) algorithm for MatLab	Liutkus et al.[38]	https://github.com/flatironinstitute/NoRMCorre
Matlab	The MathWorks, Inc	https://mathworks.com/
Image J	LOCI, University of Wisconsin	https://imagej.net/orgs/loci
IGOR Pro	WaveMetrics	https://www.wavemetrics.com/products/igorpro
Analyse Calcium Data Network script for Matlab	Smedler et al.[39]	https://github.com/EvaCher888/Matlab-scripts-for-Calcium/tree/Calcium-data
AnalyseDureeOnOff rastr script for Matlab	Github, Pierre Fontanaud and Stanislav Cherepanov	https://github.com/EvaCher888/Matlab-scripts-for-Calcium/tree/Calcium-data
Analyse FFT script for Matlab	Rubinov et al.[40]	https://github.com/EvaCher888/Matlab-scripts-for-Calcium/tree/Calcium-data
Analyse_Calcium_Data script for Matlab	Mourao et al.,[41]	https://github.com/EvaCher888/Matlab-scripts-for-Calcium/tree/Calcium-data
Analyse_Ensemble_Calcium_Data	Lee et al.[42]	https://github.com/EvaCher888/Matlab-scripts-for-Calcium/tree/Calcium-data
Multigraph script for Matlab	Github, Pierre Fontanaud and Stanislav Cherepanov	https://github.com/EvaCher888/Matlab-scripts-for-Calcium/tree/Calcium-data
Brain connectivity Toolbox	Smedler et al.[39]	https://sites.google.com/site/bctnet/
GraphPad Prism 9	GraphPad Software	https://www.graphpad.com/
R-statistical software	The R Foundation	https://www.r-project.org/
Other		
0.5mm Gradient index lens	Grintech	https://www.grintech.de/index.php?id=68&L=1

RESOURCE AVAILABILITY

Lead contact

Further information and requests should be directed to and will be fulfilled by the lead contact, Agnes O Martin (Agnes.Martin@igf.cnrs.fr).

Materials availability

This study did not generate new reagents.

Data and code availability

- All data that support findings of this study are available from the lead contact upon request.
- All code generated during work on this manuscript, available in public repository https://github.com/EvaCher888/Matlab-scripts-for-Calcium/tree/Calcium-data.
- Any additional information required to reanalyze the data in this paper is available from the lead contact upon request.

EXPERIMENTAL MODEL AND STUDY PARTICIPANT DETAILS

Mice

In the Arc, (DAT)-expressing cells, from the DAT–iCRE (DA transporter) line display an almost complete colocalization with TH expressing cells.[12,37] We crossed this line with Ai95(RCL-GCaMP6f)-D line (JAX stock #024105)[43] to study calcium activity in TIDA neurons. For *Ex vivo* experiments a total of twenty-two 6 weeks old female and eight male virgin mice were used. For *in vivo*, eleven female and eight male virgin mice in total were used. Depending on the type of experiment, mice were reused if they did not participate in pharmacology experiments (Table S1).

The stage of estrous cycle in virgin female animals, was monitored by vaginal smears. The vaginal cells were flushed by gently introducing 100 µl of saline, using a pipette. The cell suspension was deposited on a glass slide, air-dried, stained with 0.1% crystal violet stain and examined under a light microscope. Estimation of the phase of estrous cycle is based on the proportion of leucocytes, cornified epithelial cells and nucleated epithelial cells in the vaginal secretion.[44]

All mice were housed in our laboratory under standard conditions (24°C; 12h light/dark cycle, lights on at 08:00) with food and water provided *ad libitum*. All animals were treated in accordance with the principles of laboratory animal care published by the French Ethical Committee and the animal welfare guidelines of the European Community (Agreement 34.128). No statistical methods were used to pre-determine sample sizes.

METHOD DETAILS

Brain slice preparation

Virgin male or female were used in experiments. Acute coronal brain slices were used for *ex vivo* Calcium imaging experiments. Procedure was described previously.[45] Adult (>50 d old) DAT-iCRE- GCAMP6f mice were killed by rapid decapitation, between 10:00 A.M. and 12:00 P.M., after isoflurane anesthesia. Full anesthesia was confirmed by absence of response to a toe pinch. Mice were immediately decapitated. The brain was quickly removed and placed in ice-cold artificial CSF (ACSF) containing the following (in mM): 118 NaCl, 3 KCl, 11 D-glucose, 10 HEPES, 25 NaHCO3, 6 MgCl2, and 0.5 CaCl2 0.5 (osmolarity between 295 and 305 mOsm, pH 7.2 when gassed with 5% CO2 and 95% O2). The brain was then glued to the stage of a vibratome (Integraslice 7550 PSDS, Campden instruments), and 240-µm-thick coronal sections were cut. The slices were transferred at 37°C into oxygenated recording ACSF, with the same composition as above but containing 2.4 mM MgCl2 and 2.5mM CaCl2. This same solution was subsequently used for the recordings.

Ex vivo calcium imaging

Slices were immobilized with a nylon grid in a submersion chamber on the stage of an upright microscope (Discovery V12; Carl Zeiss) and superfused with oxygenated recording solution at 37°C. Brain slices were illuminated through a 20X immersion objective (W Plan Apochrome; Carl Zeiss). Calcium Imaging was performed (excitation 480 nM and emission 520nM) using an ORCA-Flash 4.0 (Hamamatsu, Japan) digital charged-coupled device camera.

Calcium imaging recordings were obtained using MetaMorph software (Molecular Devices, Sunnyvale, CA). The Ca^{2+} emission was detected every 0.5s (2Hz rate) at magnification 20X. Total time of recording was 30 minutes, with the first 10 minutes performed in aCSF, the next 10 minutes in the presence of pharmacological compound and the last 10 minutes in wash out mode. In experiments with compound application ovine PRL (oPRL) (500 ng/ml; Sigma-Aldrich) was applied.

Stereotaxic surgery

Procedure was described previously.[46] DAT-iCRE- GCAMP6f mice were anaesthetized using a mix of ketamine (100 mg/kg IP – Imalgene 1000, BOEHRINGER INGELHEIM ANIMAL HEALTH FRANCE) and xylazine (10 mg/kg IP – Rompun, ELANCO, Germany). Full anesthesia was confirmed by absence of response to a toe pinch and was monitored frequently during the surgery. After achievement of full anesthesia, the mouse was placed on the stereotaxic stage, and body temperature maintained at 37°C with a heating pad. Fur was shaved from the top of the head to the first cervical vertebrae. A lubricating ophthalmic ointment was applied to the eyes. Scalp and ears were disinfected with surgical swab using 4% iodine solution (Betadine 4%). The mouse was securely fixed on the stereotaxic frame, the scalp incised, and the fascia removed using a scalpel blade. The level of the head was confirmed by comparison of bregma and lambda. To target the Arc, the following coordinates were used: he coordinates: Rostro-caudal -1.2 mm, lateral 0.2mm and dorso-ventral -5.5mm.[47] Drilling was performed using a Brush Type H.MH-170 drill press (Foredom, CT, US) under a dissection microscope Stemi 508 (Carl Zeiss, Germany) with illumination by a

high intensity illuminator (Dolan-Jenner industries, Setra Systems inc. MA, US). A 10μl Hamilton syringe (with 30-gauge needle) was lowered to the targeted site and kept in place for 5 min to make a track for lens implantation. A 0.5mm Gradient Index (GRIN) lens (Grintech, Germany) was slowly lowered to the target area. The GRIN-lens was fixed using two-component 48% filled dental adhesive (OptiBond FL, Kerr) followed by dental cement (Tetric EvoFlow, GACD). Finally, metal wings were fixed on the top of the scalp with the GRIN-lens in center using dental cement. At the end of the surgery, the mouse was removed from the stereotaxic frame, placed in its home cage and monitored until it re-gained full consciousness.

In vivo calcium imaging

Mice were positioned in a custom-made device consisting of a running wheel and apparatus for head fixation. Strong fixation was achieved by screwing the metal wings on the head of mice onto the apparatus. GRIN lens was illuminated through a 20X objective (M Plan Apo 20, Carl Zeiss). Calcium imaging was performed (480 nM excitation and 520nM emission) using an ORCA-Flash 4.0 digital charged-coupled device camera (Hamamatsu, Japan) and an epifluorescence microscope (Discovery V12; Carl Zeiss). Calcium imaging recordings were obtained using MetaMorph software (Molecular Devices, Sunnyvale, CA). The Ca^{2+} emission was detected every 0.5sec (2Hz rate) at a 37.5X magnification. For estrous cycle monitoring, single 5-min recordings at 9.30 am each day were performed. For pharmacology experiments, the total time of each experiment was 120 minutes.

After a first 10-min control recording, recordings were performed for 5 min every 10 minutes to limit phototoxic damages. We used two approaches to induce PRL surge in the blood, i.p injection of ovine PRL and Domperidone injection. Ovine PRL is commonly used in mouse studies but is not detected by our ultrasensitive Elisa (see below), preventing the visualization of the actual rise in PRL. Due to its poor ability to penetrate the blood brain barrier,[48,49] Domperidone is known as a peripheral acting D2 receptor antagonist. It induced a surge in PRL by acting on D2 receptors located on pituitary lactotroph cells,[1] providing the opportunity to induce a surge of endogenous detectable [PRL_{blood}.].

0.1 ml of saline was injected IP immediately after the first recording to serve as control for a potential injection-induced response and then 0.1 ml of solution containing ovine PRL (500 ng/ml; Sigma-Aldrich), Domperidone (10μl/ml, Abcam) or pure saline (as control) were injected IP immediately after the 3rd recording.

Bromocriptine (40μl/ml, Tocris) was injected twice, 48 and 24 hours before recording.

Perfusion-fixation and verification of GRIN lens position

After finishing *in vivo* Calcium imaging experiments, mice were anaesthetized using mix of ketamine (100 mg/kg IP – Imalgene 1000, BOEHRINGER INGELHEIM ANIMAL HEALTH FRANCE) and xylazine (10 mg/kg IP – ELANCO, Germany). Brains were fixed by intracardiac perfusion with 4% paraformaldehyde in 0.1 M phosphate buffer, pH 7, and left overnight in the same fixative. Brains were later sliced using a vibratome and the position of the GRIN-lens was verified by microscopy (Leica).

Ultrasensitive PRL ELISA

Prolactin concentrations were measured using a home-made ELISA, as previously reported.[1] Briefly, 4-μL blood samples were withdrawn from the tail vein after *in vivo* recording (a small cut at the tip of the tail, was performed and blood was withdrawn by gently applying pressure along the tail) and diluted with 96 μL PBS-Tween 20 promptly frozen at -20°C to prevent clotting, pending analysis (PBS, 0.05% Tween20).

A 96-well plate (Sigma-Aldrich cls 9018-100EA) was coated with 50 μL capture antibody antirat PRL (anti-rPRL-IC) (National Institute of Diabetes and Digestive and Kidney Diseases (NIDDK), AFP65191 (guinea pig), NIDDK-National Hormone and Pituitary Program (NHPP; Torrance, California) at a final dilution of 1:1000 in PBS of the antibody stock solution, reconstituted in PBS as described in the data sheet (Na2HPO4 7.6mM; NaH2PO4 2.7 mM; and NaCl 0.15 M, pH 7.4). The plate was protected with Parafilm (Pechiney Plastic Packaging) and incubated at 4°C overnight in a humidified chamber. The coating antibody was decanted and 200μl of blocking buffer (5% skimmed milk powder in PBS-T was added to each well to block nonspecific binding. The plate was left for 2 hours at room temperature on a microplate shaker. In parallel, a standard curve was prepared using a 2-fold serial dilution of recombinant mouse PRL (AFP-405C; NIDDK-NHPP) in PBS-T with BSA 0.2 mg/mL (Millipore; 82-045-1). After the blocking step, the plate was washed (three times for 3 min at room temperature with PBS-T), and 50 μL of samples or standards were loaded in duplicate to the wells and incubated 2 hours at room temperature on the microplate shaker. The plate was washed, and the complex was incubated for another 90 minutes with 50μL detection antibody (rabbit anti-mouse PRL; a gift from Professor F. Talamantes, University of Santa Cruz, Santa Cruz, California) at a final dilution of 1:50 000 in blocking buffer solution. After a final wash, this complex was incubated for 90 minutes with 50 μL horseradish peroxidase conjugated antibody (anti-rabbit, IgG; Fisher Scientific; NA934) diluted in 50% PBS and 50% blocking buffer. One tablet of O-phenylenediamine (Life technologies; SAS 00-2003) was diluted into 12 mL citrate phosphate buffer (pH 5), containing 0.03% hydrogen peroxide. 100μl microliters of this substrate solution was added to each well (protected from light), and the reaction was stopped after 30 minutes with 50μLof 3M HCl. The OD from each well was determined at 490 nm using a microplate reader (Infinite 200 PRO; Tecan). An absorbance at 650 nm was used for background correction. This.

QUANTIFICATION AND STATISTICAL ANALYSIS

Calcium imaging data processing

Acquired images were corrected by X and Y axes using Non-Rigid Motion Correction (NoRMCorre) algorithm[50] in Matlab (The MathWorks, Inc.).

Corrected images were processed in Image J (LOCI, University of Wisconsin) to calculate raw fluorescence data of recorded neurons. Cells were identified by anatomical shape and fluorescence activity. GCaMP6f fluorescence reports integration of Ca^{2+} influx and clearance in the cytoplasm.[51,52] The basal calcium in cells varied greatly from highly fluorescent to undetectable. In the later, silent or sparsely firing cells are therefore not distinctly visible. Obtained data were transferred to IGOR Pro (WaveMetrics, Inc. OR, US). Debleaching and normalization algorithms were performed and normalized F/F_0 waves for each recorded cell were constructed. The first minute of recording was cut off due to intense bleaching, before performing algorithms and therefore, only the last 4 minutes of each recording were analyzed.

In vivo "silent" cells were described in case of absence of any fluorescence activity in the first control recording.

Using a modified Matlab script « Scale-Space Peak Picking »[38] named "Analyse_Calcium_Data" we determined the peaks of all waves and turned them into binary data. In more details, the algorithm determined the baseline of each wave using 9 fixed points and smoothed with "Loess" method with 30%-point windows around each point. Point to point difference between baseline and raw data was determined using the formula ∂F=calcium trace – base line. After that, each ∂F threshold was collected by 2^{nd} standard deviation of ∂F to define each peak and trough. For *ex vivo* data, elimination of false positive peaks and troughs was achieved with a general threshold calculation of the 85% percentile on all ∂F threshold collection. For *in vivo* data, due to high variability in the number of peaks and to avoid significant amount of false positive results, calibrating wave with one significant peak was added to analyze (and removed for all further calculations) and general threshold calculation of the 95% percentile was performed. The data were extracted in the form of binary information table where each frame of wave where a peak was present was indicated as "On" and if not as "Off". The total amount of frames where the waves were in "On" mode was defined as "Total time in on" and was expressed in seconds. Employing custom made Matlab script "analyseDureeOnOff rastr" we calculated the number of events (number of continuous ON frames series) and the average duration of those events. That parameter was called "Average duration in ON".

We then used binary On/Off data to calculate the frequency of ON events. For that, we utilized Fast Fourier Transformation (FFT) algorithm with computation of power spectrum.[41,53] By using custom script for Matlab "Analyse FFT". Power peak above 1% percent significance threshold obtained by 1000 of amplituded permutation of calcium trace. We analyzed 1000 random permutations of the course data. A period is considered significant if the number of power obtained by the random permutations greater than the power value associated with the period (p-value) occurs less than 1% (level of significance) of the times. Both power peaks and period, frequency (mHz) above this threshold are extracted and saved. Frequency with highest significant power was used to characterize individual wave frequency.

Figures of individual wave traces were obtained by applying F/F_0 data to "Multigraph" script in Matlab.

All recorded calcium waves were classified in 3 categories according to the duration of ON and frequency: Long (average duration in On > 1>75 seconds), short slow (Frequency <75mHz, average duration in On < 1.75 seconds) and short rapid (Frequency >75mHz, average duration in On < 1.75 seconds).

Coactive and functional networks analysis

The analysis of coactive networks was previously described by.[54] We used "Analyse_Ensemble_Calcium_Data" script for Matlab. Four inputs file were used: a zip file from ImageJ for Regions of Interest (ROI), the csv of raster ON-OFF, one projected tiff for the tissue and csv for coordinate value of the ROI center. We computed the sum of the ON-OFF from each cell in the ON-OFF raster, and generated Coactivity profile and applied 100 permutations of the original ON-OFF raster, defining a 5 % threshold for Coactivity profile. We extracted the frames of cells involved in episodes and cells involved during a coactive period above this threshold. From these data we calculated the following parameters: Total time in ensemble - total time during recording when cells were in coactive ensembles. Average duration of ensemble - calculated as mean of duration of each episode of coactivity. Number of cells per ensemble – mean number of cells participating in each ensemble. N of ensembles – total amount of not interrupted periods of cells coactivity.

Analysis of functional networks was described by.[40] Initially we obtained an adjacency matrix showing the presence of functional connections (1 for two cells connected, 0 otherwise). Cross correlation computation were carried out to measure a value of correlation between 0 and 1. The following formula was used.[40]

$$C_{ij}(\Delta t) = \frac{\sum_t (Ca_i - \overline{Ca_i})(Ca_j(t+\Delta t) - \overline{Ca_j})}{\sigma_{Ca_i}\sigma_{Ca_j}}$$

Where Ca_i and Ca_j a pair of F/F_0 for two cells in a moment of time. A fixed cut off of 0.5 value was used to filter out the correlation values.

On the functional network we used metrics measurements adapted from[42] for small size networks: Transitivity and Global Efficiency.[39,40] The Global Efficiency is an average inverse shortest path length between all pairs of nodes.[55] This measure possible to use on disconnected small size networks as we have periodically in our *in vivo* measurements.[56] Generally Global efficiency represent functional integration of network. We use next formula for calculation of Global Efficiency

$$E = \frac{1}{n}\sum_{i \in N} Ei = \frac{1}{n}\sum_{i \in N} \frac{\sum j \in Nj \neq i d_{ij}^{-1}}{n - 1}$$

Where E_i is efficiency of node i.

Transitivity is a measure of functional segregation as normalized variant of clustering coefficient (the fraction of triangles around an individual node).[57]

The following formula was used for calculation:

$$T = \frac{\sum_{i \in N} 2t_i}{\sum_{i \in N} K_i(K_i - 1)}$$

Modularity is the degree to which the network may be subdivided into such clearly delineated and nonoverlapping groups.
Modularity of the network

$$Q = \sum_{u \in M} \left[e_{uu} - \left(\sum_{v \in M} e_{uv} \right)^2 \right]$$

where the network is fully subdivided into a set of nonoverlapping modules M, and e_{uv} is the proportion of all links that connect nodes in module u with nodes in module v.[40]

We used the Brain Connectivity Toolbox for Matlab for actual calculation and "Analyse Calcium Data Network" script for Matlab ([40]). Three inputs file were used: the csv of F/F_0 waves, one projected tiff for the tissue and csv for coordinate value of the ROI center. Cross-correlation network maps were generated and obtained parameters of Global Efficiency and Transitivity were used to define the type of functional network topology.

Statistical analysis

ANOVAs of generalized linear models with post-hoc Sidak tests were used for comparisons of more than two groups. We used a Student two or one-tailed t-test for comparisons of two group and for paired data, and a Pearson correlation analysis was used when appropriate to compare the different experimental groups as indicated in the text and figure legends. Software for statistical analysis GraphPad Prism 9 (GraphPad Software, MA, USA).

We modelled each index using a cumulative links model (CLM) for ordinal data. Statistical analyses were performed on R v4.3.1 (The R Foundation). Repeated measure over time during an experiment were accounted for by including an 'individual' variable as a random effect (i.e., paired data) unless we were confronted with computational limitations (e.g. problems in variance estimations). In case of significance, post-hoc comparisons were made using *emmeans* package and p-values were adjusted for multiple comparisons (Tukey method). Probabilities were retrieved using a back-transformation of parameters. When models failed to converge, we compared indexes between groups using frequencies. For the comparisons of 2 dependent groups, a Friedman rank sum test was used. A Skillings-Mack test if some data were missing (e.g. a same score was not found between two repeated measures). For the comparison of 2 independent groups, we used a Fisher exact test.